Molecular Cell

Volume 79 Number 6 Pages 000–000 September 17, 2020

Molecular Cell

Volume 79
Number 6
September 17, 2020

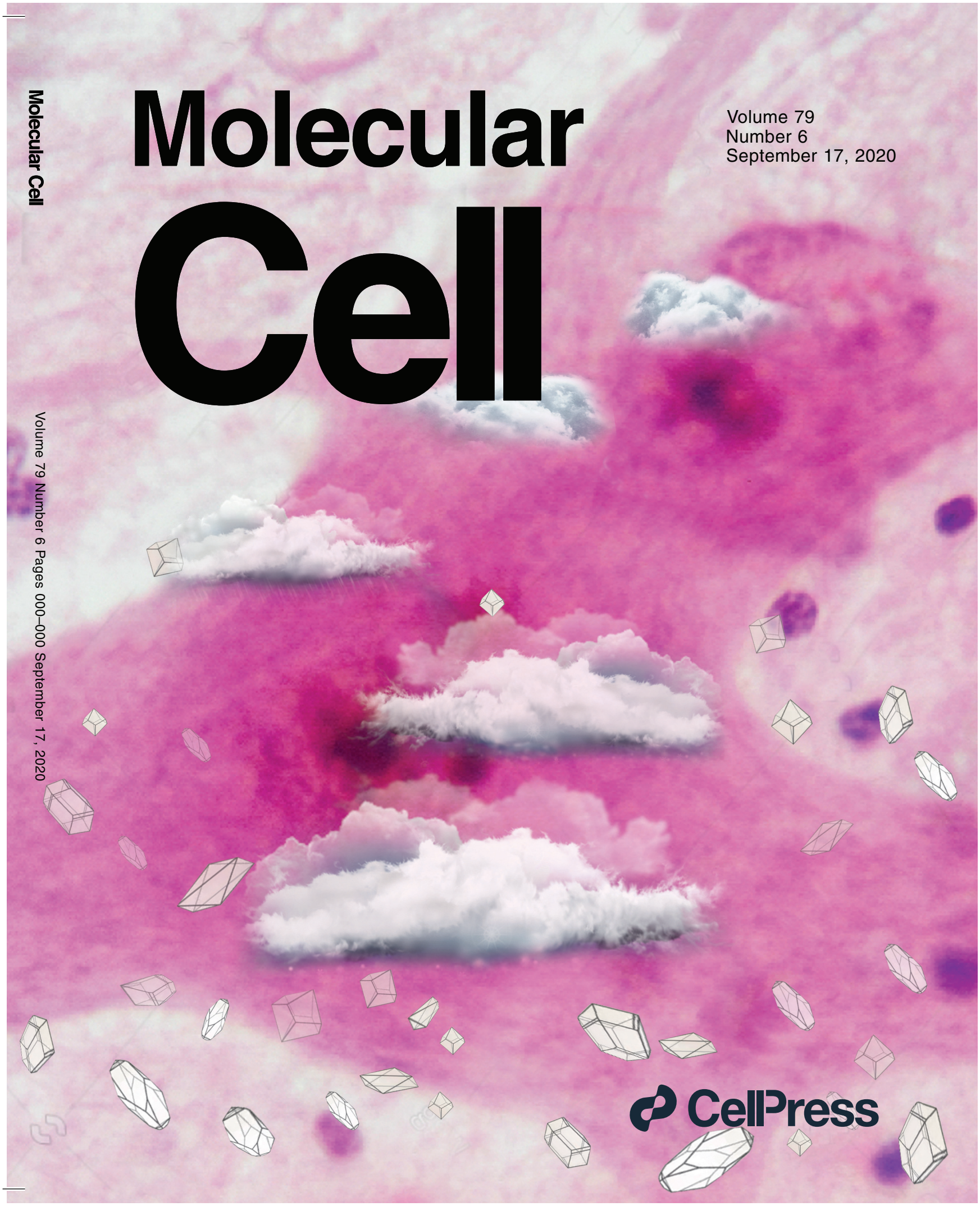

CellPress

MOLCEL_79_6.c1.indd 1 8/29/2020 5:22:04 AM

Molecular Cell

Article

Multivalent Proteins Rapidly and Reversibly Phase-Separate upon Osmotic Cell Volume Change

Graphical Abstract

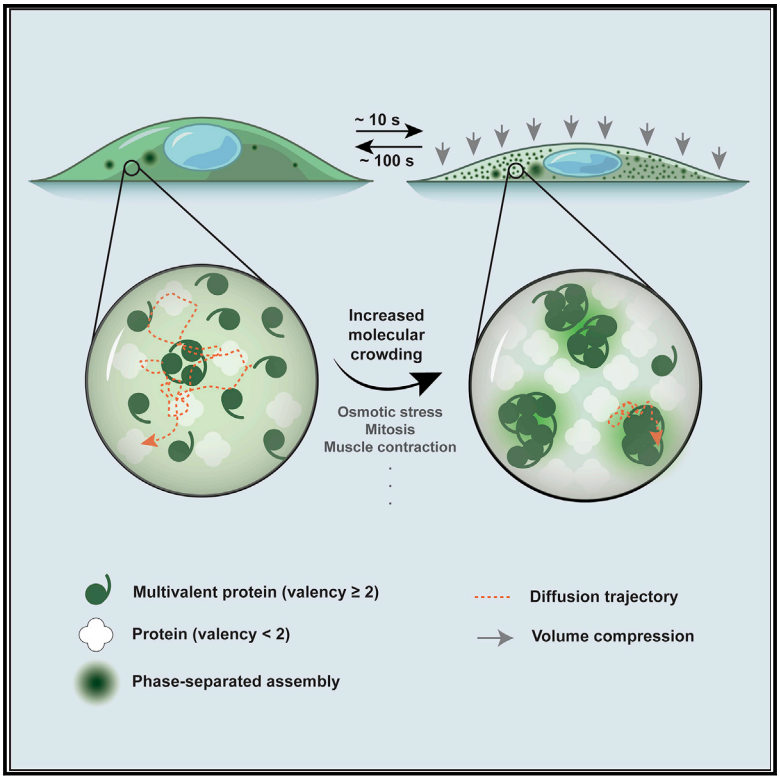

Authors

Ameya P. Jalihal, Sethuramasundaram Pitchiaya, Lanbo Xiao, ..., Mats Ljungman, Arul M. Chinnaiyan, Nils G. Walter

Correspondence

sethu@umich.edu (S.P.), arul@umich.edu (A.M.C.), nwalter@umich.edu (N.G.W.)

In Brief

Cells constantly experience osmotic variation. These external changes lead to changes in cell volume and, consequently, the internal state of molecular crowding. Jalihal and Pitchiaya et al. show that multimeric proteins respond rapidly to such cellular changes by undergoing fast and reversible phase separation.

Highlights

- DCP1A undergoes rapid and reversible hyperosmotic phase separation (HOPS)
- HOPS of DCP1A depends on the protein's trimerization domain
- Self-interacting multivalent proteins (valency ≥ 2) undergo HOPS
- HOPS of CPSF6 explains transcription termination defects during osmotic stress

Jalihal et al., 2020, Molecular Cell 79, 978–990
September 17, 2020 © 2020 Elsevier Inc.
https://doi.org/10.1016/j.molcel.2020.08.004

CellPress

CellPress

Molecular Cell

Article

Multivalent Proteins Rapidly and Reversibly Phase-Separate upon Osmotic Cell Volume Change

Ameya P. Jalihal,[1,2,12] Sethuramasundaram Pitchiaya,[3,4,10,12,*] Lanbo Xiao,[3,4] Pushpinder Bawa,[3] Xia Jiang,[3] Karan Bedi,[5] Abhijit Parolia,[3,4] Marcin Cieslik,[3,4,6] Mats Ljungman,[5,9,10,11] Arul M. Chinnaiyan,[3,4,7,8,9,10,*] and Nils G. Walter[1,9,10,13,*]

[1]Single Molecule Analysis Group, Department of Chemistry, University of Michigan, Ann Arbor, MI 48109-1055, USA
[2]Cell and Molecular Biology Graduate Program, University of Michigan, Ann Arbor, MI 48109, USA
[3]Michigan Center for Translational Pathology, University of Michigan Medical School, Ann Arbor, MI 48109-1055, USA
[4]Department of Pathology, University of Michigan, Ann Arbor, MI 48109, USA
[5]Department of Radiation Oncology, University of Michigan, Ann Arbor, MI 48109, USA
[6]Department of Computational Medicine and Bioinformatics, University of Michigan, Ann Arbor, MI 48109, USA
[7]Howard Hughes Medical Institute, University of Michigan, Ann Arbor, MI 48109, USA
[8]Department of Urology, University of Michigan, Ann Arbor, MI 48109, USA
[9]Rogel Cancer Center, University of Michigan, Ann Arbor, MI 48109, USA
[10]Center for RNA Biomedicine, University of Michigan, Ann Arbor, MI 48109, USA
[11]Department of Environmental Health Sciences, University of Michigan, Ann Arbor, MI 48109, USA
[12]These authors contributed equally
[13]Lead Contact
*Correspondence: sethu@umich.edu (S.P.), arul@umich.edu (A.M.C.), nwalter@umich.edu (N.G.W.)
https://doi.org/10.1016/j.molcel.2020.08.004

SUMMARY

Processing bodies (PBs) and stress granules (SGs) are prominent examples of subcellular, membraneless compartments that are observed under physiological and stress conditions, respectively. We observe that the trimeric PB protein DCP1A rapidly (within ~10 s) phase-separates in mammalian cells during hyperosmotic stress and dissolves upon isosmotic rescue (over ~100 s) with minimal effect on cell viability even after multiple cycles of osmotic perturbation. Strikingly, this rapid intracellular hyperosmotic phase separation (HOPS) correlates with the degree of cell volume compression, distinct from SG assembly, and is exhibited broadly by homo-multimeric (valency $\geq$ 2) proteins across several cell types. Notably, HOPS sequesters pre-mRNA cleavage factor components from actively transcribing genomic loci, providing a mechanism for hyperosmolarity-induced global impairment of transcription termination. Our data suggest that the multimeric proteome rapidly responds to changes in hydration and molecular crowding, revealing an unexpected mode of globally programmed phase separation and sequestration.

INTRODUCTION

Membraneless condensates, often referred to as membraneless organelles (MLOs), represent subcellular sites within the cytosol or nucleus of mammalian cells where key processes such as transcription, translation, post-transcriptional gene regulation, and metabolism are altered compared with the nucleoplasmic or cytoplasmic bulk (Banani et al., 2017; Spector, 2006). Misregulation of MLOs and *de novo* condensation of mutant proteins into MLOs have been strongly associated with altered gene regulation (Berchtold et al., 2018) and severe pathologies (Banani et al., 2017; Patel et al., 2015; Shin and Brangwynne, 2017). Therefore, understanding the cellular mechanisms whereby these structures assemble is critical for understanding cellular physiology and disease (Alberti, 2017; Hyman et al., 2014; Toretsky and Wright, 2014).

MLOs are hypothesized to arise from phase separation of dispersed multivalent biomolecules under specific conditions of pH, temperature, and concentration (Boeynaems et al., 2018; Hyman et al., 2014; Shin and Brangwynne, 2017). Extensive evaluation of this notion *in vitro* has defined the molecular features required to form MLOs (Hyman et al., 2014; Shin and Brangwynne, 2017; Wang et al., 2018), especially in the context of homotypic or heterotypic interactions of low-complexity domain (LCD)-containing proteins and RNAs, and has yielded an ever-expanding list of cellular components that can spontaneously phase-separate in the test tube. However, the significance of the propensity of these biomolecules to phase-separate under the physiological conditions of their native intracellular environment, where molecular crowding is dominant, is poorly understood (Alberti et al., 2019). Although it is possible to alter crowding in the test tube by addition of synthetic macromolecules (Alberti et al., 2019), the nature and extent of crowding in the cellular context is quite different (Daher et al., 2018; Walter, 2019) and changes dynamically with the cellular state. For example, cell volume adjustments occur during

processes critical for cellular homeostasis and pathology, including the cell cycle (Tzur et al., 2009; Zlotek-Zlotkiewicz et al., 2015), as well as upon cell adhesion and migration (Guo et al., 2017; Watkins and Sontheimer, 2011). Changes in cell volume and molecular crowding, frequently encountered by cells of the kidneys, liver, and gut (Lang et al., 1998), are even more rapid and dramatic during osmotic perturbation (Guo et al., 2017; Hersen et al., 2008; Miermont et al., 2013). How cells respond to rapid and frequent volume perturbations with seemingly minimal effect on their viability and whether the resulting dynamic changes in macromolecular crowding affect intracellular phase separation remains unknown.

Processing bodies (PBs) are MLOs that are constitutively present in eukaryotic cells under physiological conditions and endogenous concentrations of the constituents (Anderson and Kedersha, 2009). Their intracellular copy number has been shown to be modulated during the cell cycle (Aizer et al., 2013) and also upon prolonged (minutes to hours) hypertonic or hyperosmotic stress (Huch and Nissan, 2017), conditions that can lead to nephritic and vascular pathologies (Brocker et al., 2012). Like other environmental stressors (e.g., heat shock, oxidative stress, and metabolite deprivation), prolonged hyperosmotic stress also triggers the integrated stress response (ISR) and formation of regulatory MLOs called stress granules (SGs) (Anderson and Kedersha, 2009). Although PBs and SGs are thought to assemble via multivalent interactions between non-translating mRNAs and LCD-bearing RNA binding proteins (Van Treeck and Parker, 2018), they are compositionally distinct (Hubstenberger et al., 2017; Jain et al., 2016; Khong et al., 2017). Whether components of PBs and SGs are affected differentially by distinct stresses is largely unknown. Given that hyperosmotic stress rapidly (seconds to minutes) imparts cell volume change (Guo et al., 2017; Hersen et al., 2008; Miermont et al., 2013), it is also unclear whether the ISR and, consequently, SGs can be induced on the same timescale. Finally, the observation that PBs are regulated similarly by the cell cycle and hypertonic stress (Aizer et al., 2013; Huch and Nissan, 2017) raises the question of whether PB regulation and cell volume change may be connected.

Here we investigate the role of macromolecular crowding and cell volume change on intracellular phase separation of proteins using osmotic perturbations. We observe that DCP1A, a marker of PBs and component of the mRNA decapping machinery, rapidly (within ~10 s) undergoes cytosolic phase separation in response to hypertonic stress and that the resulting condensates dissolve over ~100 s upon return to an isotonic medium. This hyperosmotic phase separation (HOPS) can be cycled multiple times with minimal effect on cell viability and is caused by changes in cellular water content and molecular crowding. We further find that HOPS is induced by DCP1A's homo-trimerization domain and observed across a variety of cell types. Strikingly, most multimeric proteins tested with a valency of at least 2 (i.e., forming trimers and higher-order multimers but not dimers and monomers) undergo HOPS, strongly suggesting that rapid changes in hydration and molecular crowding are sensed by a significant fraction of the proteome and may lead to pleiotropic effects. Notably, G3BP and poly(A) RNA, as markers of SGs, do not undergo HOPS (as characterized by condensation within ~10 s) at their endogenous concentrations, supporting the notion that it is a unique feature of multimeric proteins. HOPS of multimeric cleavage and polyadenylation-specific factor 6 (CPSF6) in the cell's nucleus is correlated with widespread impairment of transcription termination, apparently because of sequestration of the pre-mRNA cleavage complex from a subset of transcription end sites (TESs). Our findings suggest that HOPS is a heretofore underappreciated driver of protein phase separation that rapidly senses changes in cell volume with profound effects on cellular homeostasis.

RESULTS

Changes in Extracellular Tonicity Induce Rapid and Reversible Intracellular Phase Separation of DCP1A but Not SG Markers

In a previous study (Pitchiaya et al., 2019), we observed that osmotic stress leads to phase separation of DCP1A, a non-catalytic protein component of the eukaryotic decapping complex and conserved PB marker (Anderson and Kedersha, 2009). To more broadly study the intracellular kinetics of *de novo* PB and SG formation in response to stress, we subjected U2OS cells to osmotic and oxidative stressors and performed fixed-cell protein immunofluorescence (IF) or combined IF and RNA fluorescence *in situ* hybridization (FISH) before and after the stressors (Figure 1). Under isotonic conditions (150 mM Na^+), ~9% of cellular DCP1A localized within ~10–30 foci (each ~300–800 nm in diameter) per cell, whereas G3BP protein and poly(A) RNA, as markers of SGs (Patel et al., 2015), were dispersed throughout the cytosol (Figures 1A and S1A). Upon a short (2-min) hypertonic (300 mM Na^+) shock, ~50% of cellular DCP1A, but not G3BP or poly(A) RNA, localized within ~200–300 smaller (200–300 nm) foci per cell (Figures 1A and S1A). Moreover, IF-based colocalization analysis showed that these newly formed DCP1A foci did not contain other PB markers (e.g., EDC4 and DDX6; Figure S1B), suggesting that hypertonicity-induced DCP1A foci are not *bona fide* PBs. No further changes in DCP1A focus numbers or partitioning extent were observed, even after prolonged (60-min) hypertonic treatment. At this later time point, however, G3BP and poly(A) RNA showed significant focus formation (~100–200 foci per cell, 200–300 nm in diameter; Figures 1A and S1A), in line with previous observations (Bounedjah et al., 2012), with ~13% of cellular G3BP partitioning into foci. In contrast, after 2 min of oxidative stress with sodium arsenite (SA), the numbers and partition coefficients of DCP1A foci were similar to unstressed cells, and G3BP and poly(A) RNA were still dispersed throughout the cytosol (Figures 1B and S1C). In this short time frame (2 min), the phosphorylated EIF4E (P-EIF4E)-mediated ISR was not induced by any of the stresses tested (Figure S1D). Upon prolonged (60-min) SA treatment, the number of DCP1A foci increased only marginally (~25–40 foci per cell, 300–800 nm in diameter), with a concomitant small increase in partition coefficient (~14%; Figures 1B and S1C). As expected for induction of the ISR under these conditions, G3BP and poly(A) RNA formed a small number (~18% of cellular G3BP localized in ~10–30 foci per cell) of large (400–1,100 nm in diameter) foci, and P-EIF4E was induced (Figures

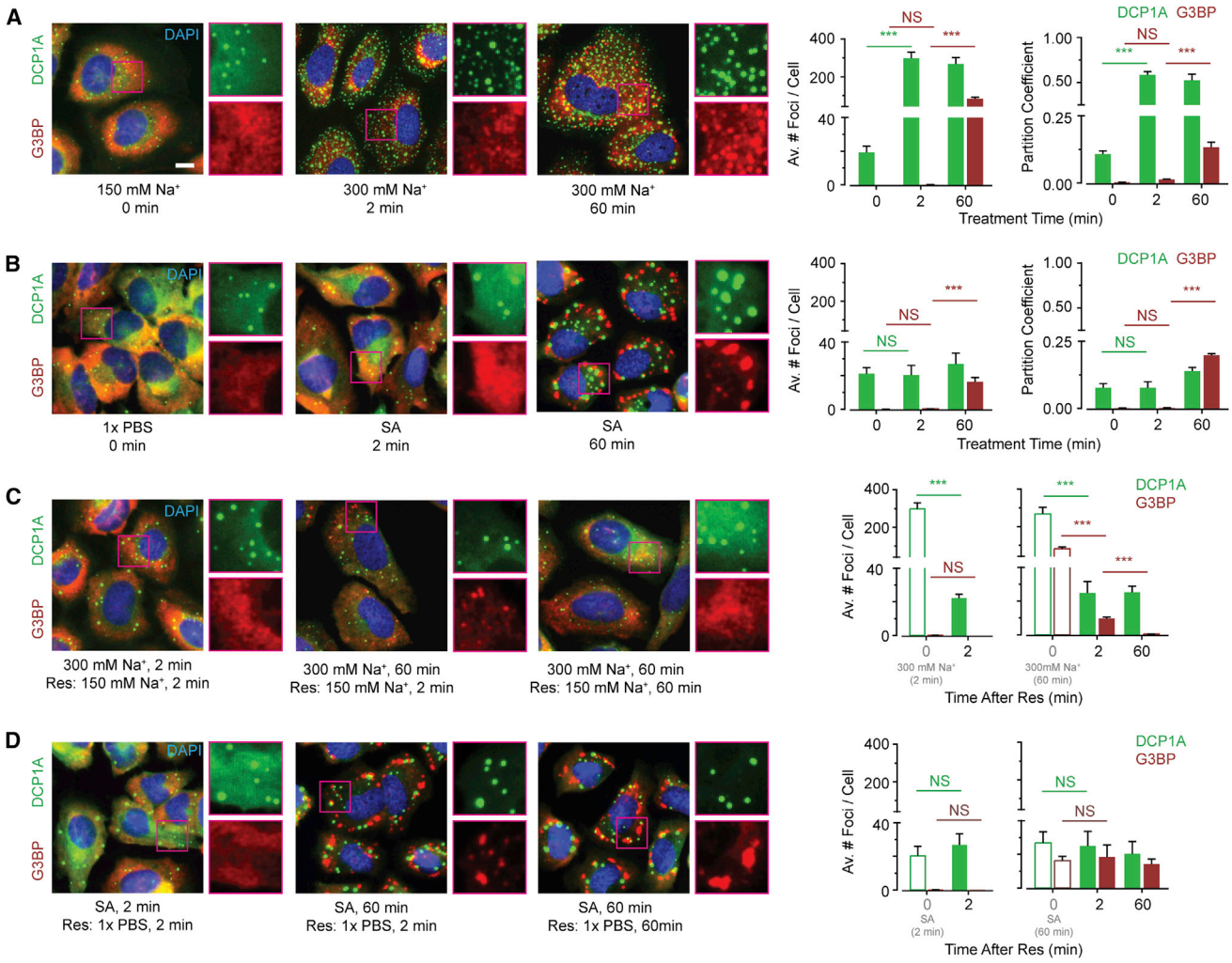

Figure 1. Extent and Kinetics of DCP1A Phase Separation during Hypertonic Stress Are Distinct from Those of the SG Marker G3BP

(A–D) Representative pseudocolored immunofluorescence (IF) images of U2OS cells stained for DAPI (blue), DCP1A (green), or G3BP (red) and the corresponding quantification of the average number of spots per cell. Scale bar, 10 μm.

(A) Cells were treated with isotonic (150 mM Na^+) or hypertonic (300 mM Na^+) medium for the appropriate time points. Quantified PCs of DCP1A and G3BP are represented in the far right panel.

(B) Cells were mock-treated with 1× PBS or treated with 0.5 mM SA for the appropriate time points. Quantified PCs of DCP1A and G3BP are represented in the far right panel.

(C) Cells were first treated with hypertonic medium (300 mM Na^+) for the appropriate time points and then rescued with isotonic (150 mM Na^+) medium for various durations. Bars with green and red outlines depict data points from (A).

(D) Cells were first treated with 0.5 mM SA for the appropriate time points and then rescued with medium containing 1× PBS for various durations. Bars with green and red outlines depict data points from (B).

Bars represent averages, and error bars represent s.e.m. n = 3, more than 60 cells, ***$p \leq 0.0001$. N.S., non-significance by two-tailed unpaired Student's t test. See also Figure S1.

1B, S1C, and S1D). Together, these data suggest that DCP1A and G3BP, when visualized in their physiological contexts, assemble into microscopically detectable foci at distinct rates and extents in response to osmotic and oxidative stressors.

Next we tested whether the increased focus numbers could be rescued by first subjecting cells to stress and subsequently recovering them in regular isotonic growth medium (Figures 1C, 1D, S1E, and S1F). We observed that hypertonicity-induced DCP1A foci disappeared rapidly, within 2 min, irrespective of the duration of the stress (Figure 1C). Although a significant fraction of the G3BP and poly(A) RNA foci also disappeared rapidly (within 2 min), the kinetics of complete recovery to baseline (i.e., pre-treatment) focus number differed from those of DCP1A (Figures 1C and S1E). In comparison, DCP1A, G3BP, and poly(A) RNA foci induced by SA stress did not disappear even after 60 min of rescue (Figures 1D and S1F). These data suggest that DCP1A and G3BP/poly(A) RNA foci show differences in the

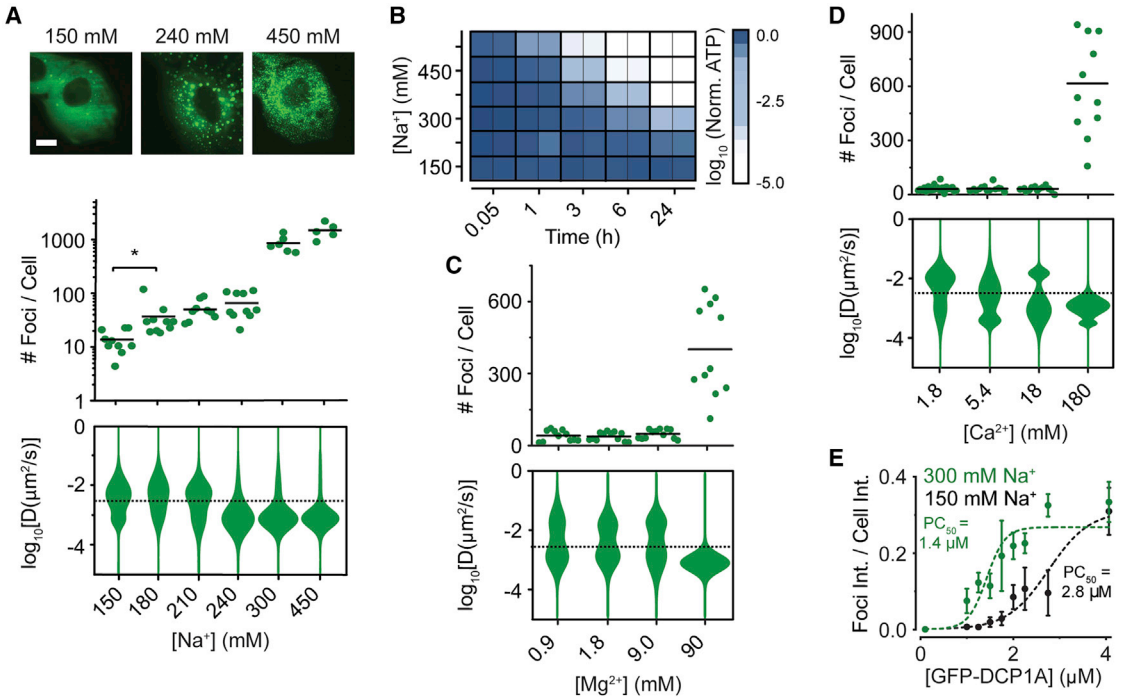

Figure 2. Physicochemical and Phenotypic Characterization of DCP1A Phase Separation during Hypertonic Stress

(A) Representative pseudocolored images of UGD cells (GFP, green) treated with growth medium containing various concentrations of Na^+ (top), scatterplot of the number of foci per cell (center), and violin plots of diffusion constants associated with DCP1A foci (bottom). n = 2, more than 5 cells per sample, *p ≤ 0.01 by two-tailed unpaired Student's t test.

(B) Representative image of a 96-well plate probed for cell viability by CellTiter-Glo assay across various Na^+ concentrations and multiple time points. n = 3 with technical replicates for each n.

(C and D) Scatterplot of the number of foci per cell (top) and violin plots of diffusion constants associated with DCP1A foci (bottom) in UGD cells treated with growth medium containing various levels of Mg^{2+} (C) or Ca^{2+} (D). n = 3, more than 5 cells per sample. The dotted line in the diffusion plots empirically demarcates high- and low-mobility fractions.

(E) Plot of PC against cellular concentration of DCP1A in samples treated with 150 mM Na^+ (light green) or 300 mM Na^+ (dark green). Points represent averages, and error bars represent standard deviation.

Data points were fitted with a dose-response curve. PC_{50}, half maximal PC. See also Figure S2.

kinetics of assembly and disassembly and that the rapid phase separation of DCP1A in response to altered tonicity is distinct from SG formation.

Hypertonicity Rapidly Induces Formation of Immobile DCP1A Condensates in Live Cells

Because fixed-cell experiments revealed that the rapid phase separation of DCP1A condensates was distinct from SG formation over minutes and hours, we decided to probe the subcellular dynamics at greater temporal resolution. To this end, we subjected the previously developed UGD cell line (a U2OS cell line that stably expresses GFP-DCP1A; Pitchiaya et al., 2019) to a systematic set of hypertonic conditions. We chose this cell line because it contains a similar number of DCP1A foci as the parental U2OS cells, and each of these foci compositionally resembles endogenous PBs (Pitchiaya et al., 2019). As a control, we first confirmed, in transiently transfected U2OS cells, that DCP1A rapidly and reversibly forms "condensates" (Banani et al., 2017) irrespective of the fluorescence tag to which it is fused (GFP, mCherry, Halo, or CLIP; Figure S2A). We noted that the condensation and rescue of SNAP-tagged DCP1A were distinct from the other tags (Figure S2A), raising the possibility that the nature of tagging might interfere with phase separation. Next, live-cell imaging of UGD cells subjected to a cycle of isotonic conditions, brief hypertonic stress, and isotonic rescue (Video S1) recapitulated the rapid and reversible nature of DCP1A phase separation (Figure 1). Furthermore, imaging of UGD cells at various levels of tonicity (150–450 mM Na^+) showed that the number of GFP-DCP1A condensates per cell rapidly and monotonically increased with salt concentration (Figure 2A); however, the mobility of the condensates, as measured by their diffusion constants, decreased. Within the time frame of treatment, typically 1–3 min, the cells remained viable across all concentrations of Na^+ and survived 225 mM Na^+ for up to 24 h (Figures 2B and S2B). Considering that many cellular processes depend on Mg^{2+} and Ca^{2+}, we next examined whether DCP1A condensation was affected by increased concentration of these divalent metal ions in the growth medium. Mg^{2+} and Ca^{2+} induced GFP-DCP1A condensation only upon a 100-fold increase over isotonic concentrations (Figures 2C and 2D), which corresponded to a significant increase in osmolarity to near double the osmolarity of isotonic growth medium (~600 mOsm/L).

These data suggest that DCP1A condensation occurs independent of the type of ion.

Biomolecular condensation scales with protein concentration (Banani et al., 2016; Sanders et al., 2020). To test whether hypertonicity-induced focus formation follows this paradigm, we calculated the partition coefficient (PC) of GFP-DCP1A as the fraction of total fluorescence within discernable foci and found that it scales linearly with focus number (Figure S2C) across a wide range of intracellular DCP1A expression levels. We observed that the intracellular concentration leading to half-maximal partitioning was significantly lower under hypertonic conditions (PC_{50} = 1.4 μM; Figure 2E) than in isotonic controls (PC_{50} = 2.8 μM), suggesting that the extent of focus formation scales with protein concentration (Figure 2E). We then wanted to find out whether differences in their cellular concentration underlie differences in hypertonicity-induced condensation of DCP1A and G3BP. To this end, we compared GFP localization across U2-OS cells that stably expressed similar levels of GFP-DCP1A (in UGD cells) or GFP-G3BP (UGG cells; Figures S2D and S2E). Upon short-term (2-min) hypertonic shock, GFP-DCP1A has a much higher focus formation potential (25-fold higher focus number and 30-fold higher PC) than GFP-G3BP. In contrast, with the exception of GFP-G3BP foci induced by prolonged SA treatment, there was markedly less focus formation in mock-treated, short-term, and long-term SA-treated controls (Figures S2D and S2E), similar to those observed in the IF assays shown in Figures 1A, 1B, S1A, and S1C. Thus, hypertonicity-induced DCP1A foci are distinct from canonical SGs at comparable cellular abundances of DCP1A and G3BP. Moreover, the rapid change in focus number occurs without a concomitant change in the total GFP fluorescence of the cell (Figure S2E), indicating that GFP-DCP1A condensation is a direct response of the existing cellular protein to osmotic perturbation rather than an indirect response of protein expression.

DCP1A Phase Separation Is Modulated by Osmotic Cell Volume Change

To distinguish between the possibilities that DCP1A condensation is a result of an increase in salt concentration or osmolarity in general, we examined the effects of two non-ionic osmolytes: sucrose and sorbitol. Subjecting UGD cells to 300 mOsm/L of either of these osmolytes supplemented to regular growth medium again resulted in formation of DCP1A condensates of lower mobility; further, cells recovered quickly when reverting to isosmotic medium (Figures 3A and S3A). These observations strongly suggest that DCP1A condensates form in response to osmotic shock rather than changes in ionic strength only.

Because hyperosmolarity is a state of increased extracellular osmotic pressure and causes cellular volume reduction by exosmosis, we hypothesized that DCP1A focus formation is the result of the increase in molecular crowding resulting from osmotic cellular shrinkage (Guo et al., 2017; Miermont et al., 2013). To test this hypothesis, we estimated volume changes of UGD cells in hyperosmotic medium using DiI staining (Sukenik et al., 2018) and 3-dimensional (3D) live-cell and fixed-cell imaging (Figures 3B, S3B, and S3C). We found that cell height, as a proxy for cell volume, rapidly (within ~1 min) and monotonically decreased over the increasing range of osmolarities in live cells with a concomitant increase in the number of DCP1A foci. This hypertonicity-induced rapid reduction in cell volume was also observed by fixed-cell 3D imaging and flow cytometry (Figures S3C and S3D) but with reduced sensitivity because of fixation-induced cell shrinkage (Ross, 1953; Su et al., 2014). Because osmotic volume change has been reported previously to be reversible in response to prolonged osmotic stress (Burg et al., 1997; Hoffmann et al., 2009), we next wanted to find out whether the regulatory volume increase occurs on the timescales where we observe formation and persistence of GFP-DCP1A condensation. However, cell height reduction in fixed cells showed little change upon prolonged hyperosmolarity, changing from ~20% (10 min) to ~25% (120 min) relative to isosmotic controls (Figure S3E), suggesting that volume recovery does not play a significant role in our system (Burg et al., 1997; Hoffmann et al., 2009). Moreover, the effect of hyperosmotic volume compression on DCP1A focus formation was independent of cell lineage (Figure S3F). Together, our data support a direct universal link between molecular crowding and GFP-DCP1A condensation.

Because DCP1A exhibits rapid and reversible condensation dependent on the degree of osmotic cell volume change, and because mammalian cells repeatedly experience such osmotic perturbations, we examined the response of UGD cells to cycling osmotic volume change (Figures 3C and 3D). UGD cells were treated for 1 min with hypertonic medium and allowed to recover for 30 min, and this treatment regimen was repeated. Quantification of the number and diffusion constants of foci across the treatment regimen showed that the timescales of DCP1A focus assembly (~10 s) and disassembly (~100 s), as well as changes in focus mobility, were highly similar across all cycles and occurred with minimal effect on cell viability (Figures 3C–3F). Hereafter we refer to this phenomenon of cytosolic DCP1A condensation as intracellular HOPS and posit that it is a cellular adaptation to osmolarity-induced changes in molecular crowding.

HOPS of DCP1A Depends on Its Trimerization Domain and Post-translational Modification Status

Macromolecular phase separation is widely thought to be driven by multivalent protein-protein and protein-nucleic acid interactions mediated by specific side-chain interactions and structures (Guo and Shorter, 2015). To investigate the underlying molecular basis of DCP1A condensation, we first tested the dependence of HOPS on different DCP1A domains. Although DCP1A does not contain any annotated nucleic acid binding domains, it contains two prominent protein interaction domains, an N-terminal EVH1 domain that interacts with the mRNA decapping protein DCP2, and a C-terminal trimerization domain that interacts with EDC3/4, a scaffolding protein of the decapping complex (Aizer et al., 2013). GFP-tagged truncation constructs of DCP1A's N-terminal domain (NTD) or C-terminal domain (CTD) were transiently transfected into U2OS cells. Upon exposing these cells to hyperosmotic shock, we observed that the CTD showed rapid and reversible condensation similar to the full-length protein. In contrast, a truncation mutant containing the NTD did not show detectable foci upon hyperosmotic shock (Figures 4A and 4B). Because the CTD mediates DCP1A trimerization and EDC4 interaction, we tested whether EDC4 is responsible for HOPS of DCP1A to narrow down the basis of condensation. Compared

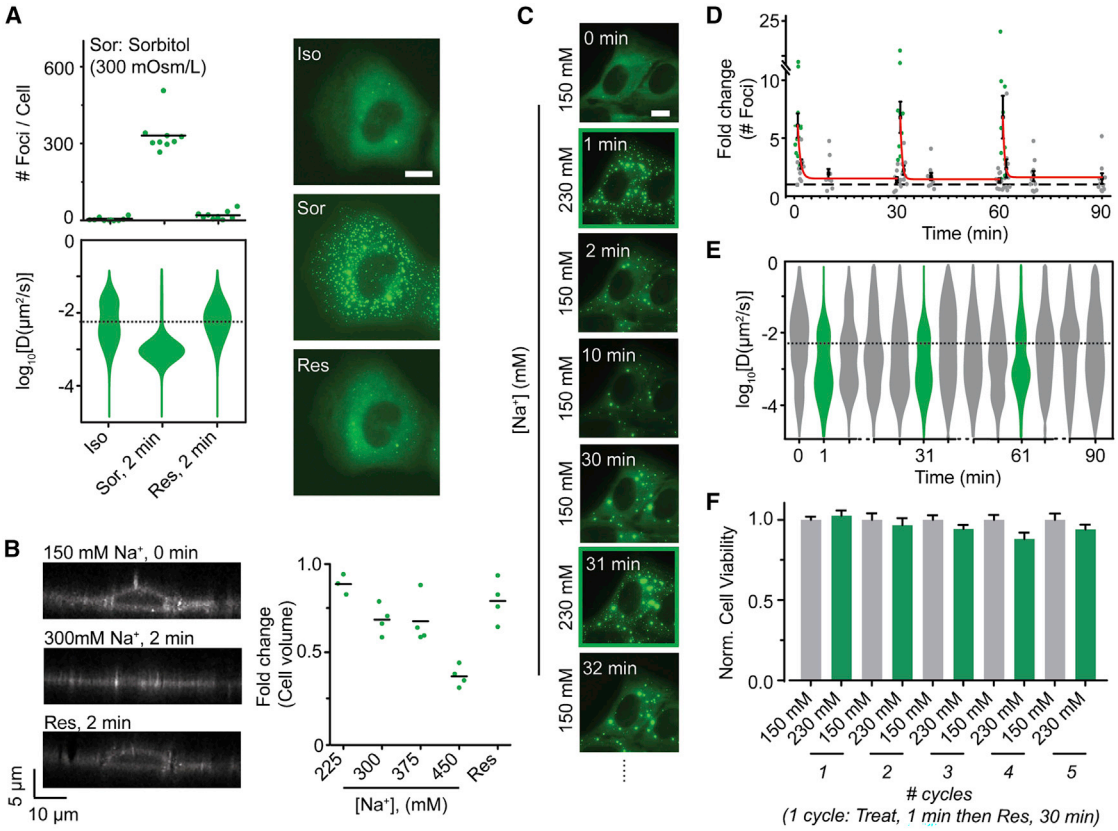

Figure 3. Hyperosmotic Compression Mediates DCP1A Phase Separation

(A) Scatterplot of the number of foci per cell (top), violin plots of diffusion constants associated with DCP1A foci (bottom), and representative pseudocolored images of UGD cells (GFP, green) treated with isosmotic (Iso) growth medium, hyperosmotic growth medium containing the non-ionic osmolyte sorbitol (Sor), or rescued with Iso medium after Sor treatment. n = 2, more than 5 cells per sample. Scale bar, 10 μm.

(B) Representative y-z projection of UGD cells (grayscale) from the 3D imaging assay, where the cells were treated with isotonic (150 mM Na^+) medium or hypertonic (300 mM Na^+) medium or rescued with isotonic medium after hypertonic treatment. n = 1, 4 cells per sample. Scale bar, 10 μm. A scatterplot of the fold change in cell volume, as normalized to the cell volume under isotonic conditions, is shown.

(C) Representative pseudocolored images of a UGD cell (GFP, green) that was treated cyclically with isotonic (150 mM Na^+) or hypertonic (300 mM Na^+) medium. Scale bar, 10 μm.

(D) Scatterplot of the fold change in focus numbers, as normalized to focus numbers in isotonic samples, associated with the assay represented in (C). The red line depicts the exponential fit. n = 2, more than 5 cells per sample. Error bars represent s.e.m.

(E) Violin plots of diffusion constants associated with DCP1A foci, associated with the assay represented in (C). n = 2, more than 5 cells per sample. The dotted line in the diffusion plots empirically demarcates high- and low-mobility fractions.

(F) Bar plots of cell viability, normalized to isotonic samples, associated with the assay represented in (C). n = 3 with 3 technical replicates for each n. Bars represent averages, and error bars represent s.e.m.

See also Figure S3.

with a scrambled (Scr) silencing RNA (siRNA) control, knockdown of EDC4 by siEDC4 resulted in reduced expression (~2-fold) of GFP-DCP1A (Figures S4A and S4B) and larger GFP-DCP1A foci under isotonic conditions (Figures 4C and 4D) but did not prevent HOPS of DCP1A. In fact, the slight reduction in HOPS of DCP1A is consistent with the ~2-fold reduced cytosolic availability of DCP1A via reduced expression and enhanced localization within large foci. These data strongly suggest that DCP1A homo-trimerization is a major driver of its HOPS.

Previous reports have suggested that PB formation can be modulated by post-translational modification (PTM), as accompanying cell cycle progression (Aizer et al., 2008). We reasoned that if a change in phosphorylation status would influence PB assembly and disassembly during the cell cycle, then such modifications should also modify the protein's response to changes in molecular crowding. We stimulated global changes in phosphorylation using a general phosphatase inhibitor (PI), okadaic acid, or the c-Jun N-terminal kinase inhibitor (KI) SP600125 on UGD cells (Aizer et al., 2013), which we found to modulate DCP1A phosphorylation levels (Figure S4C). Although the PI did not significantly alter HOPS of GFP-DCP1A compared with a DMSO-treated control, the KI significantly increased the number of newly formed immobile condensates (Figure 4E). Additionally, PI treatment mediated a significant reduction in the mobility of DCP1A condensates even after rescuing the cells with isotonic medium (Figure 4E). Together, these observations suggest that PTMs

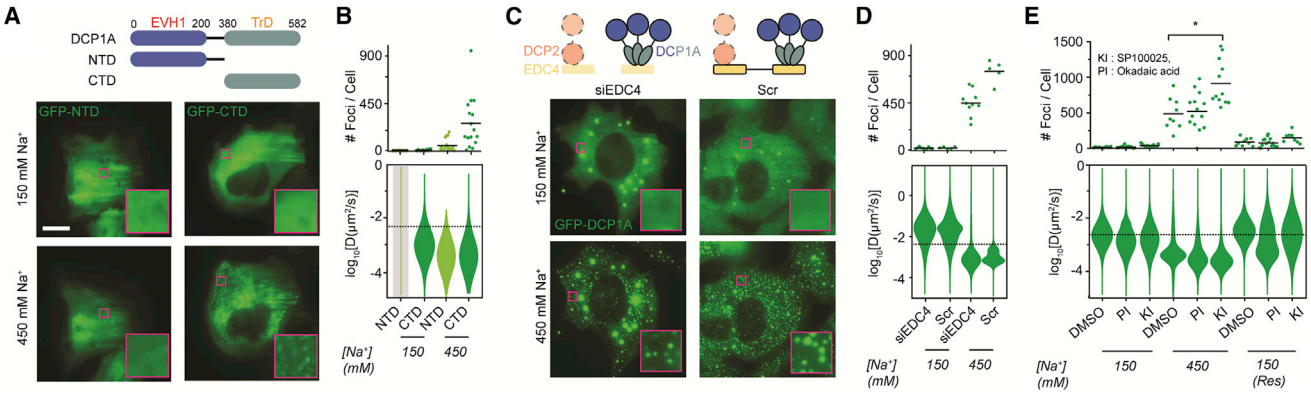

Figure 4. HOPS of DCP1A Is Dependent on Its Trimerization Domain and Modulated by PTMs but Not Its Interaction with EDC4

(A) Schematic of full-length DCP1A, NTD, or CTD constructs (top, not to scale). The EVH1 domain, trimerization domain, and amino acid numbers are marked. Shown are representative pseudocolored images of U2OS cells (GFP, green) transfected with GFP-NTD or GFP-CTD that were treated with isotonic (150 mM Na^+) or hypertonic (300 mM Na^+) medium (bottom). Scale bar, 10 μm.

(B) Scatterplot of the number of foci per cell (top) and violin plots of diffusion constants associated with DCP1A foci (bottom) imaged in (A). n = 3, more than 5 cells per sample.

(C) Schematic of DCP1A, DCP2, and EDC4 in the decapping complex (top, not to scale) under siEDC4 or Scr treatment conditions. Representative pseudocolored images of siEDC4- or Scr siRNA-treated UGD cells (GFP, green) treated with isotonic (150 mM Na^+) or hypertonic (300 mM Na^+) medium (bottom). Scaled as in (A).

(D) Scatterplot of the number of foci per cell (top) and violin plots of DCP1A diffusion constants (bottom), associated with assay represented in (C). n = 3, more than 5 cells per sample.

(E) Scatterplot of the number of foci per cell (top) and violin plots of DCP1A diffusion constants (bottom) in UGD cells that were pre-treated treated with DMSO, KI, or PI and imaged in isotonic (150 mM Na^+) medium, hypertonic (300 mM Na^+) medium, or rescued with isotonic medium after hypertonic treatment. n = 3, more than 5 cells per sample.

The dotted line in the diffusion plots empirically demarcates high- and low-mobility fractions. See also Figure S4.

can modulate HOPS of proteins, likely by altering surface charges on which protein-protein interactions depend.

Multimeric Proteins with a Valency of at Least 2 Generally Exhibit HOPS

Considering that the minimally required structural determinant of HOPS of DCP1A is only its trimerization domain (Figure 4), we reasoned that other self-interacting proteins with multimerization domains might also exhibit HOPS. We performed an unbiased high-throughput IF analysis of 104 endogenous proteins and 4 nucleic acid-based targets (m6A, RNA-DNA hybrid poly-ADP-ribose, and rRNA) in U2OS cells subjected to short-term osmotic stress (Figures 5A, 5B, and S5A; Table S1). Because antibodies may exhibit cross-reactivity and impaired access to some proteins in osmotically compressed cells, we complemented high-throughput IF analysis by imaging osmotically perturbed U2OS cells transiently transfected with GFP-tagged proteins (Figures 5C, S5B, and S5C; Table S2; STAR Methods). A combined analysis of both assays showed that proteins annotated as multimers or homo-oligomers (by Gene Ontology) that were trimers or larger had a higher propensity to exhibit HOPS (Figures 5C–5E). Monomeric proteins (e.g., GFP), dimeric proteins (e.g., TP53 and AKT), and several proteins without annotated multimerization domains (e.g., PARP13) did not exhibit HOPS (65 of 75 targets; Figures 5C–5E). In contrast, a significant fraction (18 of 29 annotated homo-oligomers) of multimeric proteins with a self-interaction valence of 2 or more (i.e., trimers and other higher-order multimers, including LCD-bearing proteins such as DCP1A, HSF1, PKM2, PAICS, FUS, and TDP43) as well as several proteins with no known multimerization domain (e.g., ERp72) exhibited HOPS (Figures 5C–5E and S5). In some cases, we observed the disappearance of foci upon hyperosmotic shock, which rapidly reformed upon isotonic rescue (e.g., CDK12; Figures 5B and S5A). These observations support the hypothesis that multimeric proteins with a self-interaction valency of 2 or more generally undergo HOPS. Overall, our data suggest that the subcellular distribution of a significant fraction of the cellular proteome, 16% of which is annotated to be self-interacting (Pérez-Bercoff et al., 2010), appears to be altered by osmotic compression. Our findings thus support a widespread and pervasive effect of HOPS on subcellular organization.

We next tested whether hetero-multimers exhibit HOPS by using live-cell imaging of cells co-expressing Halo-tagged DCP1A and GFP-tagged interactors of DCP1A. Although overexpression of GFP-AGO2, which co-localizes with DCP1A at PBs, and GFP-DCP2, which directly interacts with DCP1A, by themselves failed to induce HOPS, high co-expression with Halo-DCP1A induced GFP-AGO2 and GFP-DCP2 condensates that colocalized with DCP1A HOPS condensates (Figure S6). Notably, using GFP-DCP1A and Halo-DCP1A co-expression as a positive control showed significantly higher HOPS propensity, as expected for DCP1A, whereas GFP by itself failed to undergo condensation under any condition (Figure S6). We conclude that trimeric DCP1A is sufficient to drive formation of these condensates but that HOPS can also be induced via hetero-multimerization dependent on the extent of interaction and concentration of the interactors. At endogenous concentrations of PB constituents, DCP1A HOPS condensates may primarily represent DCP1A protein (Figure S1B).

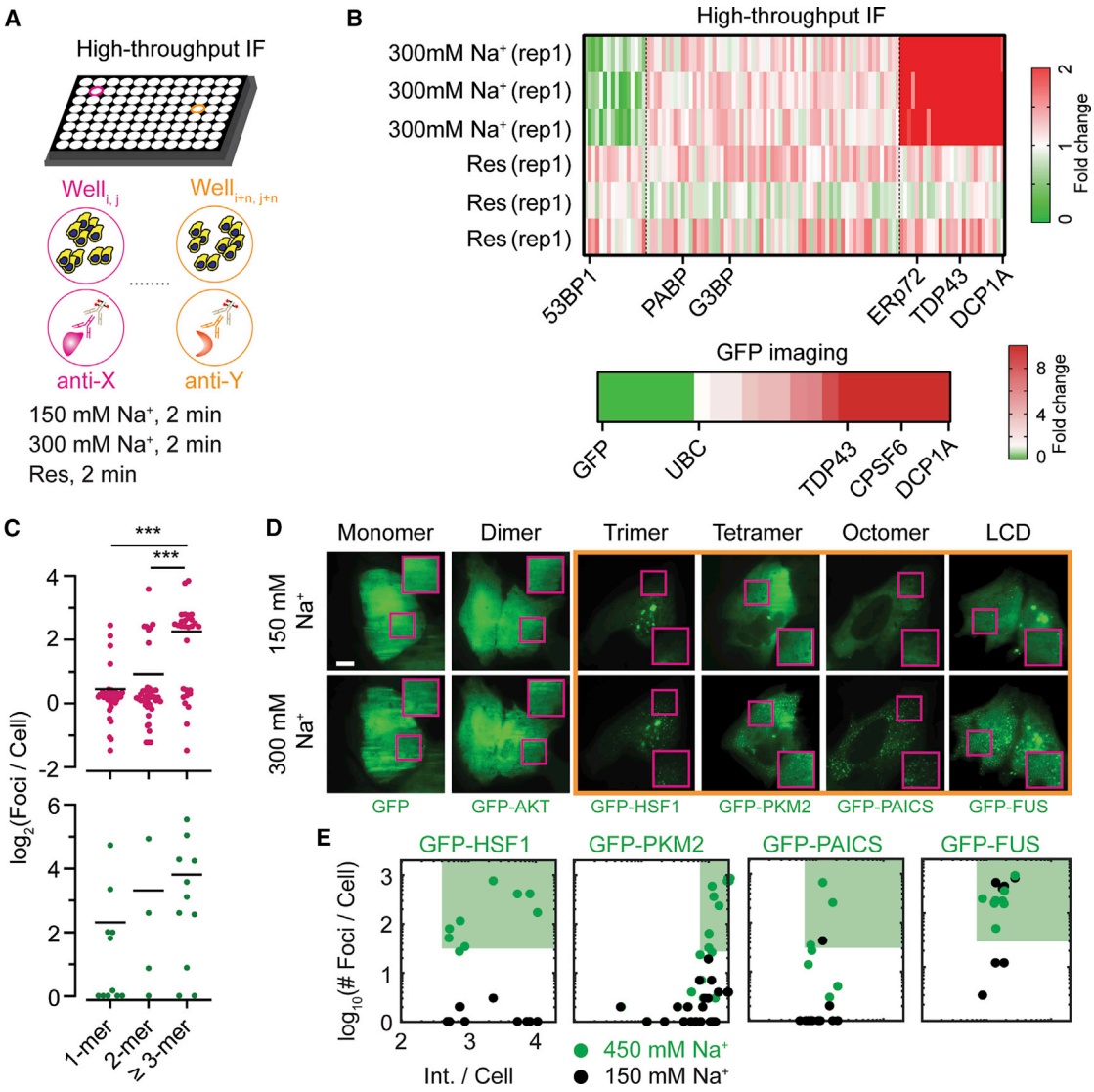

Figure 5. High-Throughput IF and GFP Imaging Show that Several Multimeric Proteins of a Valency of 2 or More Generally Exhibit HOPS

(A) Schematic of the high-throughput IF assay.

(B) Heatmap representing the fold change in spot number of the 108 targets tested by high-throughput IF, as normalized to isotonic conditions. rep, replicates. A heatmap representing the fold change in spot number of 22 protein targets tested by GFP imaging, normalized to isotonic conditions, is shown below.

(C) Scatterplot of the average number of foci per cell as a function of known protein multimerization ability. Each dot represents an individual target in the high-throughput IF (top) or the GFP imaging assay (bottom). n = 3, ***$p \leq 0.0001$ by two-tailed, unpaired Student's t test.

(D) Representative pseudocolored images of U2OS cells (GFP, green) transfected with the appropriate GFP-tagged construct and treated with isotonic (150 mM Na^+) medium or hypertonic (300 mM Na^+) medium. Scale bar, 10 μm. The inset depicts a magnified area corresponding to a 15 × 15 μm^2 magenta box. The orange box encloses proteins that exhibit HOPS.

(E) Scatterplot of the number of foci per cell against the area-normalized cell intensity for each protein. n = 2, more than 5 cells per sample. The green contour depicts the HOPS regimen.

See also Figures S5 and S6.

HOPS of CPSF6 Is Correlated with Hyperosmolarity-Induced Impairment of Transcription Termination

One of the positive hits in high-throughput IF and GFP imaging was CPSF6 (Figures 5B and 6A), a structural component of the cleavage- and polyadenylation-specific factors (CPSFs)-containing complex (Elkon et al., 2013), which mediates 3′ end formation of transcripts. Prior reports have shown that impaired function of CPSFs during hyperosmotic stress is correlated with transcription termination defects in certain cellular lineages, leading to continued transcription of regions downstream of annotated genes (Vilborg et al., 2015). We posited that sequestration of CPSF6 from transcription sites by HOPS mediates transcription termination defects under hyperosmotic stress. To test this hypothesis, we assessed the effect of hyperosmolarity on the

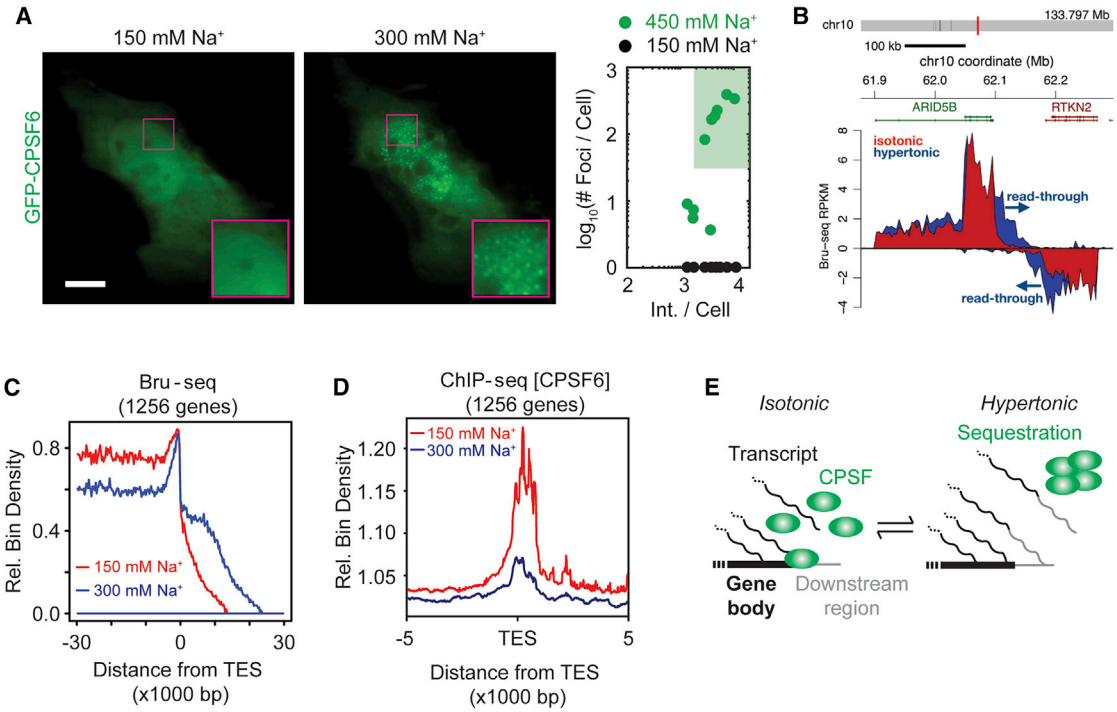

Figure 6. HOPS of CPSF6 Is Correlated with Impaired Transcription Termination

(A) Representative pseudocolored images of a U2OS cell transfected with GFP-CPSF6 (green) incubated with isotonic (150 mM Na^+, red) medium and then treated with hypertonic (300 mM Na^+, blue) medium for 1 min. Scale bar, 10 μm.

(B) Bru-seq tracks across the ARID5B and RTKN2 genes showing transcriptional read-through of the TES.

(C) Aggregate nascent RNA Bru-seq enrichment profile across TESs. Relative bin density of ~1,256 genes, with expression >0.5 RPKM and length >30 kb, exhibiting a ~10-kb average extension of reads past the TES, in response to hypertonic conditions for 30 min. Samples were prepared from cells treated with isotonic (150 mM Na^+, red) or hypertonic (300 mM Na^+, blue) medium for 30 min.

(D) Aggregated ChIP-seq peaks of CPSF6 around the TES under hypertonic (300 mM Na^+, blue) and isotonic conditions (300 mM Na^+, red).

(E) Schematic model of transcription termination defect induced by HOPS of CPSFs.

See also Figure S7.

nascent transcriptome, which is expected to be sensitive to termination defects, using nascent-state RNA sequencing of transcripts by 5-bromouridine metabolic labeling and sequencing (Bru-seq) and BruChase-seq after 30 min of hyperosmotic stress (Paulsen et al., 2014). We found that, indeed, the read density of sequences downstream of TESs was significantly higher in hypertonic samples than under isotonic conditions (Figures 6B, 6C, and S7A). Performing steady-state RNA sequencing (RNA-seq) of UGD cells subjected to prolonged (4-h) osmotic perturbations revealed that hyperosmotic stress also had a pervasive long-term effect that, strikingly, was reversed upon rescuing cells from hypertonic shock with isotonic medium (Figures S7B and S7C). Chromatin immunoprecipitation followed by sequencing (ChIP-seq) further showed that elongating RNA polymerase II (RNA Pol II) was enriched downstream of canonical TESs specifically in hyperosmotic samples, consistent with transcription proceeding beyond the TESs (Figure S7D). In addition, ChIP-seq analysis of the CPSF proteins CPSF1, CPSF6, and CPSF73 (Figures 6D, S6E, and S6F; STAR Methods) showed that localization of CPSF complexes at TESs was reduced significantly under hyperosmotic conditions. Taken together, a model emerges by which rapid formation of HOPS condensates of CPSF6 sequesters CPSF activity away from chromatin, leading to functional impairment of cleavage and polyadenylation at the TES of a subset of transcripts upon hyperosmotic stress (Figure 6D).

DISCUSSION

In this study, we report multiscale (i.e., cellular, subcellular, and molecular) characterization of a seemingly widespread intracellular phase separation phenomenon in response to hyperosmotic stress, here called HOPS (Figure 7). We find that a significant fraction of the multimeric proteome undergoes rapid and reversible intracellular redistribution into phase-separated condensates during osmotic cell volume change. Empirically, proteins with a self-interaction valency of 2 or more exhibit HOPS in response to changes in cell volume, and these changes are intricately linked to altered hydration and molecular crowding during hyperosmotic stress.

Exosmosis Leads to a Protein Concentration Increase, Molecular Dehydration, and HOPS

Intracellular water expelled upon hyperosmotic compression (i.e., exosmosis) is thought to originate from "free" water

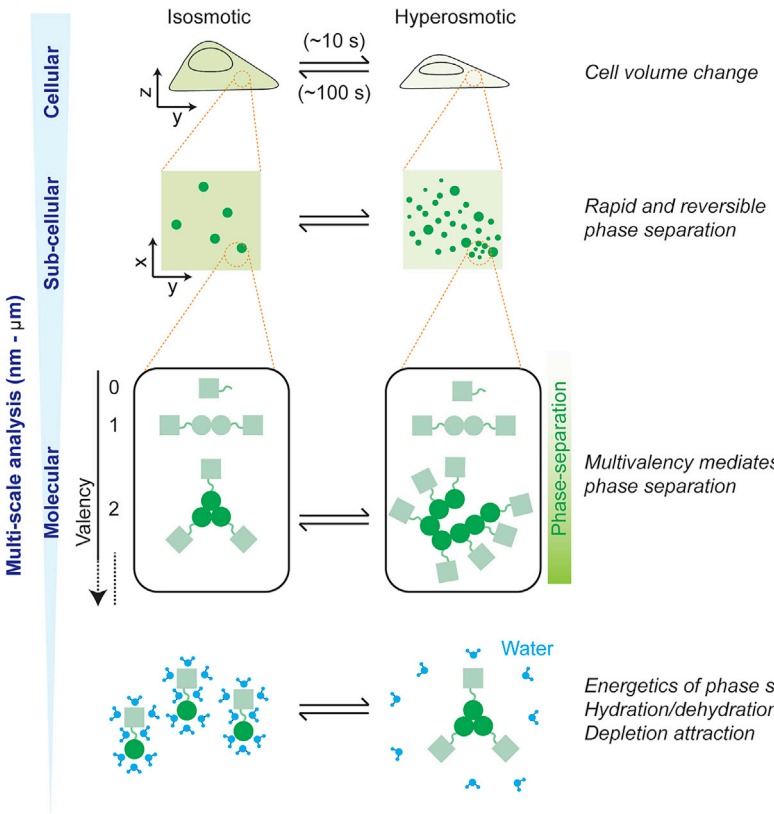

Figure 7. Model of the Multiscale Features of HOPS

Our multi-scale analysis shows that HOPS of multimeric proteins is mediated by concerted changes in cell volume, macromolecular crowding, and hydration.

molecules that constitute the bulk of the cell and water molecules bound to cellular solutes and involved in macromolecular solvation (Ball, 2017). On one hand, loss of free water upon exosmosis leads to cell volume loss and a concomitant increase in cellular concentration that will shift the monomer-multimer equilibrium of a protein toward multimerization, facilitated by forces like depletion attraction (Marenduzzo et al., 2006). On the other hand, loss of bound water results in decreased protein hydration, which may lead to protein precipitation by increasing surface exposure of hydrophobic regions (Muschol and Rosenberger, 1997). Rehydration rapidly replenishes both types of water molecules to shift the monomer-multimer equilibrium back toward the solvated monomer, dissolving the condensate.

It is thought that hydrophobic patches found in homo-multimeric proteins can spontaneously interact upon hydration loss or ''dewetting'' (Jensen et al., 2003; Liu et al., 2005), whereas the phase separation driven by LCDs and RNAs is posited to involve larger interaction networks (Wang et al., 2018). The high speed and high reversibility of HOPS of multimeric proteins is consistent with the former mechanism, where hydrophobic patches of homo-oligomeric proteins promote association into condensates (Krainer et al., 2020; Figure 7). The cost in translational entropy of individual diffusing molecules upon condensation into such large, slowly diffusing complexes is expected to be compensated by the enthalpic gain of hydrophobic patch association.

Features and Functional Consequences of Widespread Intracellular HOPS

We observe that increasing intracellular crowding ~2-fold (based on the up to ~2-fold change in cell height) leads to formation of a large number of DCP1A condensates with greatly reduced mobility; further, cellular volume recovery readily reverses the condensation and decreased mobility (Figures 2 and 3). Additionally, we find that the cellular concentration of the protein monomer affects the size and number of condensates (Figure S4D). The latter observation implies that, under low-protein-concentration conditions, our ability to identify proteins undergoing HOPS may be limited by our fluorescence microscope's resolution. A conservative estimate, based on cytoplasmic redistribution of GFP signal into hyperosmotic condensates (Figures S2D and S2E), suggests that we can detect 10-mers and any higher-order condensates. This level of sensitivity has allowed us to use IF to curate a high-confidence list of endogenous proteins that do and do not undergo HOPS (Figure 5). Thus, we can define the protein features that govern HOPS, primarily the requirement for a homo-multimerization domain of a valency of 2 or more that is common among cellular proteins.

It is becoming increasingly clear that excluded volume effects mediated by molecular crowding affect macromolecular structure, protein stability, enzyme activity, and nucleo-cytoplasmic organization (Daher et al., 2018; Delarue et al., 2018; Hancock, 2004; Minton, 2001; Sukenik et al., 2018). Previous work has noted the potential for phase separation to dynamically buffer intracellular protein concentration (Alberti et al., 2019). More directly, we find that the structural pre-mRNA cleavage and polyadenylation factor CPSF6 (Elkon et al., 2013) undergoes nuclear HOPS, which we observe to be correlated with transcriptome-wide functional impairment of transcription termination (Figure 6).

HOPS May Serve as a Rapid Cellular Sensor of Volume Compression

The rapid timescales of hyperosmotic cell volume compression, volume recovery under isotonicity, and cell viability after multiple osmotic cycles (Figures 2 and 3) we observe concur with prior reports of cell volume changes (Guo et al., 2017; Hersen et al., 2008; Miermont et al., 2013). Our data, which indicate that even a 20% reduction in cell volume by osmotic compression can mediate HOPS, point to the high sensitivity of the multimeric

proteome toward volume changes. Our findings are consistent with the notion that the eukaryotic proteome is delicately balanced near the threshold of phase separation (Walter and Brooks, 1995; Wilson, 1899). In fact, it stands to reason that the interaction energies and concentrations of homo-multimeric proteins may have evolved to facilitate crossing of their individual phase separation thresholds only when cellular conditions demand.

Notably, our HOPS-associated cell volume changes are comparable with the rapid volume changes that occur during cell adhesion and migration through confined spaces (Guo et al., 2017; Watkins and Sontheimer, 2011) as well as those associated with the cell cycle (Tzur et al., 2009). Incidentally, homeostatic processes that may be expected to suppress phase separation, such as PTMs and allosteric effects by metabolically compatible osmolytes, operate over the timescales (minutes to hours) of the cell cycle. Consistent with this expectation, we find that loss of phosphorylation enhances the extent of HOPS (Figure 4).

Perhaps the most striking aspect of HOPS is its rapid onset, which is faster than the rate of assembly of stress response-associated granules (Wheeler and Hyman, 2018). This feature is similar to recent reports of rapid nuclear condensation of the DEAD-box RNA helicase DDX4 in response to environmental stress (Nott et al., 2015) and the transcriptional co-activator YAP in response to hyperosmotic stress (Cai et al., 2019) and may be homologous to a similar phenomenon reported in yeast (Alexandrov et al., 2019). Notably, prolonged exposure to hyperosmotic conditions, similar to other environmental stressors, triggers the ISR and subsequent assembly of SGs, often localized adjacent to pre-formed DCP1A condensates or PBs (Figure 1; Kedersha et al., 2005). These observations support a model whereby homo-multimeric proteins serve as "first responders" of osmotic compression because of the sensitivity of protein complex formation to changes in crowding (Sukenik et al., 2017). Such early volume sensors may be critical for suspending cellular biochemistry until appropriate protective or corrective action has been initiated. This escalating response may be critical because osmotic changes in the environment are unpredictable and can rapidly fluctuate but have widespread implications in an array of physiological and disease contexts. For instance, cells in the renal medulla frequently and rapidly experience high salt concentrations, resulting in up to four times the osmolarity of serum during urine production (Lang et al., 1998). Extreme dehydration can lead to hypernatremia, a state of serum hyperosmolarity characterized by Na^+ levels exceeding 145 mM over extended periods of time, which is associated with pervasive physiological dysfunction (Nilsson and Sunnerhagen, 2011). During such prolonged stress, initiation of the ISR may lead to long-term adaptation. In the latter case, long-lasting condensates of the protein WNK1, which, notably, is also a homo-multimer, have been observed in viable kidneys of mice raised on high-K^+ diets (Boyd-Shiwarski et al., 2018).

Acute and prolonged HOPS are reversible (Figure 1) and can mediate widespread effects, including impairment of transcription termination (Figure 6; Vilborg et al., 2015), YAP-programmed transcription initiation (Cai et al., 2018), inhibition of ribosomal translocation (Wu et al., 2019), modulation of RNA silencing (Pitchiaya et al., 2019), and altered degradation of ribosomal proteins (Yasuda et al., 2020), all of which potentially contribute to cell survival. Although other mechanisms may also be at play, protein sequestration away from the site of their function provides a straightforward biophysical explanation for many of these effects (Figure 6). In fact, such a mechanism may also explain the defects in transcription termination observed in cells exposed to prolonged heat shock (Cardiello et al., 2018), suggesting that protein sequestration might be a common mechanism across multiple stress responses. Additionally, rapid formation of rigid condensates may aid in maintaining the structural integrity of cell by altering physical forces in the crowded interior (Quiroz et al., 2020). Future studies will help us to better understand the connection between MLO formation and protective cellular mechanisms, as heralded here.

STAR★METHODS

Detailed methods are provided in the online version of this paper and include the following:

- KEY RESOURCE TABLE
- RESOURCE AVAILABILITY
  - Lead Contact
  - Materials Availability
  - Data and Code Availability
- EXPERIMENTAL MODEL AND SUBJECT DETAILS
  - Cell lines
- METHOD DETAILS
  - DNA and RNA oligonucleotides
  - Plasmids
  - Cell viability assays
  - Immunofluorescence
  - Combined IF and RNA fluorescence *in situ* hybridization
  - Microscopy
  - Image Analysis
  - Flow cytometry
  - RNA-seq and Bru-seq
  - Chromatin Immunoprecipitation followed by sequencing (ChIP-seq) and analysis.
- QUANTIFICATION AND STATISTICAL ANALYSIS

SUPPLEMENTAL INFORMATION

Supplemental Information can be found online at https://doi.org/10.1016/j.molcel.2020.08.004.

ACKNOWLEDGMENTS

A.P.J. was supported by NIH T-32-GM007315. S.P. was supported by an AACR prostate cancer research fellowship and an NCI-SPORE Career Enhancement Award. A.M.C. is an NCI Outstanding Investigator, Howard Hughes Medical Institute Investigator, A. Alfred Taubman Scholar, and American Cancer Society Professor. This work was supported by NIH grant R01 GM122803 and a University of Michigan Comprehensive Cancer Center/Bio-interfaces Institute research grant (to N.G.W.) and NCI Prostate SPORE (P50 CA186786 to A.M.C.). We thank X. Cao, F. Su, and R. Wang for technical assistance with sequencing library preparation, M. Paulsen for assistance with Bru-seq assays, and M. Denies for help with some initial experiments. We also acknowledge NSF MRI-ID grant DBI-0959823 (to N.G.W.) for seeding the

Single Molecule Analysis in Real-Time (SMART) Center, whose Single Particle Tracker TIRFM equipment was used for much of this study with support from J.D. Hoff. Finally, we would like to thank N. Kedersha and Y. Shav-Tal for several plasmids.

AUTHOR CONTRIBUTIONS

S.P. conceived the study. A.P.J. performed all live-cell imaging experiments. S.P. and X.J. performed all fixed-cell assays and phenotypic analyses. L.X. constructed several plasmids. A.P., P.B., K.B., M.C., and M.L. performed and analyzed the sequencing assays. S.P., A.P.J., A.M.C., and N.G.W. designed the study. S.P., A.P.J., N.G.W., and A.M.C. wrote the manuscript, and all authors provided feedback on the manuscript.

DECLARATION OF INTERESTS

The authors declare no competing interests.

Received: October 14, 2019
Revised: June 11, 2020
Accepted: August 5, 2020
Published: August 27, 2020

REFERENCES

Aizer, A., Brody, Y., Ler, L.W., Sonenberg, N., Singer, R.H., and Shav-Tal, Y. (2008). The dynamics of mammalian P body transport, assembly, and disassembly in vivo. Mol. Biol. Cell *19*, 4154–4166.

Aizer, A., Kafri, P., Kalo, A., and Shav-Tal, Y. (2013). The P body protein Dcp1a is hyper-phosphorylated during mitosis. PLoS ONE *8*, e49783.

Alberti, S. (2017). Phase separation in biology. Curr. Biol. *27*, R1097–R1102.

Alberti, S., Gladfelter, A., and Mittag, T. (2019). Considerations and Challenges in Studying Liquid-Liquid Phase Separation and Biomolecular Condensates. Cell *176*, 419–434.

Alexandrov, A.I., Grosfeld, E.V., Dergalev, A.A., Kushnirov, V.V., Chuprov-Netochin, R.N., Tyurin-Kuzmin, P.A., Kireev, I.I., Ter-Avanesyan, M.D., Leonov, S.V., and Agaphonov, M.O. (2019). Analysis of novel hyperosmotic shock response suggests 'beads in liquid' cytosol structure. Biol. Open *8*, bio044529.

Anderson, P., and Kedersha, N. (2009). RNA granules: post-transcriptional and epigenetic modulators of gene expression. Nat. Rev. Mol. Cell Biol. *10*, 430–436.

Ball, P. (2017). Water is an active matrix of life for cell and molecular biology. Proc. Natl. Acad. Sci. USA *114*, 13327–13335.

Banani, S.F., Rice, A.M., Peeples, W.B., Lin, Y., Jain, S., Parker, R., and Rosen, M.K. (2016). Compositional Control of Phase-Separated Cellular Bodies. Cell *166*, 651–663.

Banani, S.F., Lee, H.O., Hyman, A.A., and Rosen, M.K. (2017). Biomolecular condensates: organizers of cellular biochemistry. Nat. Rev. Mol. Cell Biol. *18*, 285–298.

Berchtold, D., Battich, N., and Pelkmans, L. (2018). A Systems-Level Study Reveals Regulators of Membrane-less Organelles in Human Cells. Mol. Cell *72*, 1035–1049.e5.

Boeynaems, S., Alberti, S., Fawzi, N.L., Mittag, T., Polymenidou, M., Rousseau, F., Schymkowitz, J., Shorter, J., Wolozin, B., Van Den Bosch, L., et al. (2018). Protein Phase Separation: A New Phase in Cell Biology. Trends Cell Biol. *28*, 420–435.

Bounedjah, O., Hamon, L., Savarin, P., Desforges, B., Curmi, P.A., and Pastré, D. (2012). Macromolecular crowding regulates assembly of mRNA stress granules after osmotic stress: new role for compatible osmolytes. J. Biol. Chem. *287*, 2446–2458.

Boyd-Shiwarski, C.R., Shiwarski, D.J., Roy, A., Namboodiri, H.N., Nkashama, L.J., Xie, J., McClain, K.L., Marciszyn, A., Kleyman, T.R., Tan, R.J., et al. (2018). Potassium-regulated distal tubule WNK bodies are kidney-specific WNK1 dependent. Mol. Biol. Cell *29*, 499–509.

Brocker, C., Thompson, D.C., and Vasiliou, V. (2012). The role of hyperosmotic stress in inflammation and disease. Biomol. Concepts *3*, 345–364.

Burg, M.B., Kwon, E.D., and Kültz, D. (1997). Regulation of gene expression by hypertonicity. Annu. Rev. Physiol. *59*, 437–455.

Cai, D., Sukenik, S., Feliciano, D., Gruebele, M., and Lippincott-Schwartz, J. (2018). Phase Separation of YAP Reprograms Cells for Long-term YAP Target Gene Expression. Nat. Cell Biol. *21*, 1578–1589.

Cai, D., Feliciano, D., Dong, P., Flores, E., Gruebele, M., Porat-Shliom, N., Sukenik, S., Liu, Z., and Lippincott-Schwartz, J. (2019). Phase separation of YAP reorganizes genome topology for long-term YAP target gene expression. Nat. Cell Biol. *21*, 1578–1589.

Cardiello, J.F., Goodrich, J.A., and Kugel, J.F. (2018). Heat Shock Causes a Reversible Increase in RNA Polymerase II Occupancy Downstream of mRNA Genes, Consistent with a Global Loss in Transcriptional Termination. Mol. Cell. Biol. *38*, e00181–18.

Daher, M., Widom, J.R., Tay, W., and Walter, N.G. (2018). Soft Interactions with Model Crowders and Non-canonical Interactions with Cellular Proteins Stabilize RNA Folding. J. Mol. Biol. *430*, 509–523.

Delarue, M., Brittingham, G.P., Pfeffer, S., Surovtsev, I.V., Pinglay, S., Kennedy, K.J., Schaffer, M., Gutierrez, J.I., Sang, D., Poterewicz, G., et al. (2018). mTORC1 Controls Phase Separation and the Biophysical Properties of the Cytoplasm by Tuning Crowding. Cell *174*, 338–349.e20.

Elkon, R., Ugalde, A.P., and Agami, R. (2013). Alternative cleavage and polyadenylation: extent, regulation and function. Nat. Rev. Genet. *14*, 496–506.

Guo, L., and Shorter, J. (2015). It's Raining Liquids: RNA Tunes Viscoelasticity and Dynamics of Membraneless Organelles. Mol. Cell *60*, 189–192.

Guo, M., Pegoraro, A.F., Mao, A., Zhou, E.H., Arany, P.R., Han, Y., Burnette, D.T., Jensen, M.H., Kasza, K.E., Moore, J.R., et al. (2017). Cell volume change through water efflux impacts cell stiffness and stem cell fate. Proc. Natl. Acad. Sci. USA *114*, E8618–E8627.

Hancock, R. (2004). A role for macromolecular crowding effects in the assembly and function of compartments in the nucleus. J. Struct. Biol. *146*, 281–290.

Herrmann, C.J., Schmidt, R., Kanitz, A., Artimo, P., Gruber, A.J., and Zavolan, M. (2020). PolyASite 2.0: a consolidated atlas of polyadenylation sites from 3′ end sequencing. Nucleic Acids Res. *48* (D1), D174–D179.

Hersen, P., McClean, M.N., Mahadevan, L., and Ramanathan, S. (2008). Signal processing by the HOG MAP kinase pathway. Proc. Natl. Acad. Sci. USA *105*, 7165–7170.

Hoffmann, E.K., Lambert, I.H., and Pedersen, S.F. (2009). Physiology of cell volume regulation in vertebrates. Physiol. Rev. *89*, 193–277.

Hubstenberger, A., Courel, M., Benard, M., Souquere, S., Ernoult-Lange, M., Chouaib, R., Yi, Z., Morlot, J.B., Munier, A., Fradet, M., et al. (2017). P-Body Purification Reveals the Condensation of Repressed mRNA Regulons. Mol. Cell *68*, 144–157.e5.

Huch, S., and Nissan, T. (2017). An mRNA decapping mutant deficient in P body assembly limits mRNA stabilization in response to osmotic stress. Sci. Rep. *7*, 44395.

Hyman, A.A., Weber, C.A., and Jülicher, F. (2014). Liquid-liquid phase separation in biology. Annu. Rev. Cell Dev. Biol. *30*, 39–58.

Jain, S., Wheeler, J.R., Walters, R.W., Agrawal, A., Barsic, A., and Parker, R. (2016). ATPase-Modulated Stress Granules Contain a Diverse Proteome and Substructure. Cell *164*, 487–498.

Jensen, T.R., Østergaard Jensen, M., Reitzel, N., Balashev, K., Peters, G.H., Kjaer, K., and Bjørnholm, T. (2003). Water in contact with extended hydrophobic surfaces: direct evidence of weak dewetting. Phys. Rev. Lett. *90*, 086101.

Kedersha, N., Stoecklin, G., Ayodele, M., Yacono, P., Lykke-Andersen, J., Fritzler, M.J., Scheuner, D., Kaufman, R.J., Golan, D.E., and Anderson, P. (2005). Stress granules and processing bodies are dynamically linked sites of mRNP remodeling. J. Cell Biol. *169*, 871–884.

Khong, A., Matheny, T., Jain, S., Mitchell, S.F., Wheeler, J.R., and Parker, R. (2017). The Stress Granule Transcriptome Reveals Principles of mRNA Accumulation in Stress Granules. Mol. Cell *68*, 808–820.e5.

Krainer, G., Welsh, T.J., Joseph, J.A., Espinosa, J.R., Sridhar, A., Toprakcioglu, Z., Gudiškytė, G., Czekalska, M.A., Arter, W.E., et al. (2020). Reentrant liquid condensate phase of proteins is stabilized by hydrophobic and non-ionic interactions. bioRxiv. https://doi.org/10.1101/2020.05.04.076299.

Lang, F., Busch, G.L., Ritter, M., Völkl, H., Waldegger, S., Gulbins, E., and Häussinger, D. (1998). Functional significance of cell volume regulatory mechanisms. Physiol. Rev. *78*, 247–306.

Li, H., and Durbin, R. (2009). Fast and accurate short read alignment with Burrows-Wheeler transform. Bioinformatics *25*, 1754–1760.

Li, H., Handsaker, B., Wysoker, A., Fennell, T., Ruan, J., Homer, N., Marth, G., Abecasis, G., and Durbin, R.; 1000 Genome Project Data Processing Subgroup (2009). The Sequence Alignment/Map format and SAMtools. Bioinformatics *25*, 2078–2079.

Liu, P., Huang, X., Zhou, R., and Berne, B.J. (2005). Observation of a dewetting transition in the collapse of the melittin tetramer. Nature *437*, 159–162.

Marenduzzo, D., Finan, K., and Cook, P.R. (2006). The depletion attraction: an underappreciated force driving cellular organization. J. Cell Biol. *175*, 681–686.

Miermont, A., Waharte, F., Hu, S., McClean, M.N., Bottani, S., Léon, S., and Hersen, P. (2013). Severe osmotic compression triggers a slowdown of intracellular signaling, which can be explained by molecular crowding. Proc. Natl. Acad. Sci. USA *110*, 5725–5730.

Minton, A.P. (2001). The influence of macromolecular crowding and macromolecular confinement on biochemical reactions in physiological media. J. Biol. Chem. *276*, 10577–10580.

Model, M.A. (2018). Methods for cell volume measurement. Cytometry A *93*, 281–296.

Muschol, M., and Rosenberger, F. (1997). Liquid-liquid phase separation in supersaturated lysozyme solutions and associated precipitate formation/crystallization. J. Chem. Phys. *107*, 1953–1962.

Nilsson, D., and Sunnerhagen, P. (2011). Cellular stress induces cytoplasmic RNA granules in fission yeast. RNA *17*, 120–133.

Nott, T.J., Petsalaki, E., Farber, P., Jervis, D., Fussner, E., Plochowietz, A., Craggs, T.D., Bazett-Jones, D.P., Pawson, T., Forman-Kay, J.D., and Baldwin, A.J. (2015). Phase transition of a disordered nuage protein generates environmentally responsive membraneless organelles. Mol. Cell *57*, 936–947.

Patel, A., Lee, H.O., Jawerth, L., Maharana, S., Jahnel, M., Hein, M.Y., Stoynov, S., Mahamid, J., Saha, S., Franzmann, T.M., et al. (2015). A Liquid-to-Solid Phase Transition of the ALS Protein FUS Accelerated by Disease Mutation. Cell *162*, 1066–1077.

Paulsen, M.T., Veloso, A., Prasad, J., Bedi, K., Ljungman, E.A., Magnuson, B., Wilson, T.E., and Ljungman, M. (2014). Use of Bru-Seq and BruChase-Seq for genome-wide assessment of the synthesis and stability of RNA. Methods *67*, 45–54.

Pérez-Bercoff, A., Makino, T., and McLysaght, A. (2010). Duplicability of self-interacting human genes. BMC Evol. Biol. *10*, 160.

Pitchiaya, S., Androsavich, J.R., and Walter, N.G. (2012). Intracellular single molecule microscopy reveals two kinetically distinct pathways for microRNA assembly. EMBO Rep. *13*, 709–715.

Pitchiaya, S., Krishnan, V., Custer, T.C., and Walter, N.G. (2013). Dissecting non-coding RNA mechanisms in cellulo by Single-molecule High-Resolution Localization and Counting. Methods *63*, 188–199.

Pitchiaya, S., Heinicke, L.A., Park, J.I., Cameron, E.L., and Walter, N.G. (2017). Resolving Subcellular miRNA Trafficking and Turnover at Single-Molecule Resolution. Cell Rep. *19*, 630–642.

Pitchiaya, S., Mourao, M.D.A., Jalihal, A.P., Xiao, L., Jiang, X., Chinnaiyan, A.M., Schnell, S., and Walter, N.G. (2019). Dynamic Recruitment of Single RNAs to Processing Bodies Depends on RNA Functionality. Mol. Cell *74*, 521–533.e6.

Quiroz, F.G., Fiore, V.F., Levorse, J., Polak, L., Wong, E., Pasolli, H.A., and Fuchs, E. (2020). Liquid-liquid phase separation drives skin barrier formation. Science *367*, eaax9554.

Ramírez, F., Ryan, D.P., Grüning, B., Bhardwaj, V., Kilpert, F., Richter, A.S., Heyne, S., Dündar, F., and Manke, T. (2016). deepTools2: a next generation web server for deep-sequencing data analysis. Nucleic Acids Res. *44* (W1), W160-5.

Ross, K.F.A. (1953). Cell Shrinkage caused by Fixatives and Paraffin-wax Embedding in Ordinary Cytological Preparations. J. Cell Sci. *s3-94*, 125–139.

Sanders, D.W., Kedersha, N., Lee, D.S.W., Strom, A.R., Drake, V., Riback, J.A., Bracha, D., Eeftens, J.M., Iwanicki, A., Wang, A., et al. (2020). Competing Protein-RNA Interaction Networks Control Multiphase Intracellular Organization. Cell *181*, 306–324.e28.

Shin, Y., and Brangwynne, C.P. (2017). Liquid phase condensation in cell physiology and disease. Science *357*, 1253.

Spector, D.L. (2006). SnapShot: Cellular bodies. Cell *127*, 1071.

Su, J.W., Hsu, W.C., Tjiu, J.W., Chiang, C.P., Huang, C.W., and Sung, K.B. (2014). Investigation of influences of the paraformaldehyde fixation and paraffin embedding removal process on refractive indices and scattering properties of epithelial cells. J. Biomed. Opt. *19*, 75007.

Sukenik, S., Ren, P., and Gruebele, M. (2017). Weak protein-protein interactions in live cells are quantified by cell-volume modulation. Proc. Natl. Acad. Sci. USA *114*, 6776–6781.

Sukenik, S., Salam, M., Wang, Y., and Gruebele, M. (2018). In-Cell Titration of Small Solutes Controls Protein Stability and Aggregation. J. Am. Chem. Soc. *140*, 10497–10503.

Toretsky, J.A., and Wright, P.E. (2014). Assemblages: functional units formed by cellular phase separation. J. Cell Biol. *206*, 579–588.

Tzur, A., Kafri, R., LeBleu, V.S., Lahav, G., and Kirschner, M.W. (2009). Cell growth and size homeostasis in proliferating animal cells. Science *325*, 167–171.

Van Treeck, B., and Parker, R. (2018). Emerging Roles for Intermolecular RNA-RNA Interactions in RNP Assemblies. Cell *174*, 791–802.

Vilborg, A., Passarelli, M.C., Yario, T.A., Tycowski, K.T., and Steitz, J.A. (2015). Widespread Inducible Transcription Downstream of Human Genes. Mol. Cell *59*, 449–461.

Walter, N.G. (2019). Biological Pathway Specificity in the Cell-Does Molecular Diversity Matter? BioEssays *41*, e1800244.

Walter, H., and Brooks, D.E. (1995). Phase separation in cytoplasm, due to macromolecular crowding, is the basis for microcompartmentation. FEBS Lett. *361*, 135–139.

Wang, J., Choi, J.M., Holehouse, A.S., Lee, H.O., Zhang, X., Jahnel, M., Maharana, S., Lemaitre, R., Pozniakovsky, A., Drechsel, D., et al. (2018). A Molecular Grammar Governing the Driving Forces for Phase Separation of Prion-like RNA Binding Proteins. Cell *174*, 688–699.e16.

Watkins, S., and Sontheimer, H. (2011). Hydrodynamic cellular volume changes enable glioma cell invasion. J. Neurosci. *31*, 17250–17259.

Wheeler, R.J., and Hyman, A.A. (2018). Controlling compartmentalization by non-membrane-bound organelles. Philos. Trans. R. Soc. Lond. B Biol. Sci. *373*, 20170193.

Wilson, E.B. (1899). The Structure of Protoplasm. Science *10*, 33–45.

Wu, C.C., Zinshteyn, B., Wehner, K.A., and Green, R. (2019). High-Resolution Ribosome Profiling Defines Discrete Ribosome Elongation States and Translational Regulation during Cellular Stress. Mol. Cell *73*, 959–970.e5.

Yasuda, S., Tsuchiya, H., Kaiho, A., Guo, Q., Ikeuchi, K., Endo, A., Arai, N., Ohtake, F., Murata, S., Inada, T., et al. (2020). Stress- and ubiquitylation-dependent phase separation of the proteasome. Nature *578*, 296–300.

Zlotek-Zlotkiewicz, E., Monnier, S., Cappello, G., Le Berre, M., and Piel, M. (2015). Optical volume and mass measurements show that mammalian cells swell during mitosis. J. Cell Biol. *211*, 765–774.

STAR★METHODS

KEY RESOURCE TABLE

REAGENT or RESOURCE	SOURCE	IDENTIFIER
Antibodies		
Information about 112 antibodies used in this study are listed in Table S1	N/A	N/A
Chemicals, Peptides, and Recombinant Proteins		
MAP Kinase Inhibitor SP100025	Invivogen	tlrl-sp60
Okadaic acid, sodium salt	EMD Millipore	459620-25UG
DiI stain	Thermo-Fisher	D3911
Sodium (meta) Arsenite	Sigma	S7400-100G
JaneliaFluor 549 HaloTag ligand	Promega	GA1110
CLIP-Cell 505 ligand	NEB	S9217S
SNAP-Cell 647-SiR	NEB	S9102S
Crystal Violet (Certified Biological Stain)	Thermo-Fisher	C581-100
Formaldehyde	Sigma-Aldrich	F8775-25ML
Critical Commercial Assays		
Fugene HD	Promega	E2311
Lipofectamine 2000	Thermo-Fisher	11668027
CellTiter-Glo® Luminescent Cell Viability Assay	Promega	G7570
HighCell ChIP-Protein G kit	Diagenode	C01010063
iPure Kit V2	Diagenode	C03010015
KAPA Hyper Prep Kit	KAPABiosystems	KK8500
KAPA Pure beads	Roche	07983280001
Phusion DNA Polymerase	NEB	M0530S
Deposited Data		
Raw image data	Mendeley Data	Mendeley Data: https://doi.org/10.17632/pwnmg77wmb.2
RNA sequencing data	GEO	GEO: GSE154123; GEO: GSE156228
Experimental Models: Cell Lines		
Human: U2-OS	ATCC	HTB-96
Human: HK-2	ATCC	CRL-2190
Human: Caki-1	ATCC	HTB-46
Human: U2-OS stably expressing GFP-DCP1A (UGD)	Pitchiaya et al., 2019	N/A
Human: U2-OS stably expressing GFP-G3BP (UGG)	From Nancy Kedersha	N/A
Oligonucleotides		
Ambion negative control siRNA 1	Thermo-Fisher	AM4611
siRNA targeting EDC4 SMARTPool (siEDC4)	Dharmacon	M-016635-00-0005
Recombinant DNA		
Information about 30 plasmids used in this study are listed in Table S2	N/A	N/A
Software and Algorithms		
MATLAB 8.3	The Mathworks Inc.	R2014a
Prizm 7.04	GraphPad	Prizm 7.04
Origin 2018	OriginLab	Origin 2018
Imaris 9.1.0	Bitplane AG	Imaris 9.1.0
Fiji	ImageJ/NIH	Fiji

(*Continued on next page*)

Continued

REAGENT or RESOURCE	SOURCE	IDENTIFIER
Custom MATLAB routines	This paper	N/A
Custom ImageJ macros	This paper	N/A
Bacterial and viral strains		
XL10-Gold Ultracompetent Cells	Agilent	200315

RESOURCE AVAILABILITY

Lead Contact

Further information and requests for resources and reagents should be directed to the Lead Contact, Nils G. Walter (nwalter@umich.edu) and corresponding author Sethuramasundaram Pitchiaya (sethu@umich.edu).

Materials Availability

This study did not generate any unique reagents.

Data and Code Availability

The accession number for the Bru-seq data reported in this paper is GSE: GSE154123. The accession number for the RNA-seq and ChIP sequencing data reported in this paper is GSE: GSE156228. Raw image data have been deposited to Mendeley Data: https://doi.org/10.17632/pwnmg77wmb.2.

EXPERIMENTAL MODEL AND SUBJECT DETAILS

Cell lines

U2-OS (HTB-96, ATCC), U2-OS-GFP-DCP1A (UGD) and Caki-1 (HTB-46, ATCC) cells were propagated in McCoy's 5A medium (GIBCO, # 16600) supplemented with 10% fetal bovine serum (GIBCO, # 16000) and Penicillin-Streptomycin (GIBCO, #15140) at 37°C under 5% CO_2. UGD cells were kept under positive selection with 100 μg/mL G418. HK2 (CRL-2190, ATCC) cells were cultured in Keratinocyte Serum Free Medium (K-SFM 17005042, ATCC) supplemented with 0.05 mg/mL Bovine Pituitary Extract and 5 ng/mL epidermal growth factor provided with the K-SFM kit. Hypertonic medium was prepared by supplementing regular growth medium with 10x PBS such that the appropriate sodium concentration was achieved. Isotonic medium was prepared by mock supplementing regular growth medium with 1x PBS, whose volumes matched that of 10x PBS in hypertonic medium. Oxidative stress was induced by treating cells with 0.5 mM sodium arsenite ($NaAsO_2$, SA). Hyperosmotic medium with sucrose or sorbitol were prepared by directly dissolving the appropriate reagent to achieve 300 mOsm/L (300 mM). Plasmid transfections for GFP imaging were achieved using Fugene HD (Promega, # E2311) as per the manufacturer's protocol. UGD cells were transfected with siRNAs using Lipofectamine RNAimax (Thermo-Fisher, # 13778030) as per the manufacturer's protocol. For live cell imaging of Halo-DCP1A, CLIP-DCP1A, and SNAP-DCP1A, cells were treated with 100 nM of the appropriate ligand for 30 min in growth medium without phenol-red. After the treatment, cells were washed three times in phenol-red free McCoy's 5A medium (GE-Amersham, # SH3027001) and placed back in the incubator for 30 min, prior to imaging. For live cell imaging, cells were imaged in phenol-red free medium containing 1% FBS and the appropriate tonicity.

For DCP1A expression time course data (Figure S2B), U2OS cells were transfected with pGFP-DCP1A using Fugene HD. Transfected cells were imaged at 12, 24, 36, and 48 hours after transfection to allow the expression level of the protein to build up. Cells were images under isotonic and hypertonic conditions at each time point to cover about 2-orders of magnitude of total GFP fluorescence intensity.

METHOD DETAILS

DNA and RNA oligonucleotides

DNA oligonucleotide with 30 consecutive T's (Oligo-dT36-Cy5) contained a Cy5 dye at the 3′ end and was purchased from IDT. Dyes were attached after oligonucleotide synthesis to a 3′ amino group on a C6 carbon linker and were HPLC purified by the vendor. Negative control siRNA (Scr, Ambion negative control siRNA 1) and siRNA against EDC4 (siEDC4, siRNA targeting EDC4 SMARTPool) were purchased as ready-to-use duplexes from Thermo-Fisher and Dharmacon respectively.

Plasmids

Most plasmids were purchased from Addgene or were shared by independent labs. GFP-tagged protein candidates were selected based on gene ontology annotation containing terms ''identical protein binding'' (GO:0042802), ''protein homotrimerization'' (GO:0070207), ''protein trimerization'' (GO:0070206), ''protein dimerization'' (GO:0046983) and ''protein tetramerization''

(GO:0051262) and independently verified for their self-interacting ability by the tool SLIPPER (http://lidong.ncpsb.org/slipper/index_1.html). The resulting pools of proteins were selected to cover a range of valences. The proteins tested in each class are: monomeric, p53; dimeric, AKT, Rac2; trimeric, HSF1; tetrameric, PKM2; octomeric, PAICS; IDR-containing: FUS, TDP-43. pcDH-Halo-DCP1A, pcDH-SNAP-DCP1A, pcDH-GFP-DCP1A, pcDH-mCherry-DCP1A, and pcDH-CLIP-DCP1A were constructed by first sub-cloning the DCP1A open-reading frame (ORF) from pEGFP-DCP1A into the pcDH backbone to generate pcDH-DCP1A. The ORFs of Halo, SNAP, GFP, mCherry and CLIP were PCR amplified from pFN21A (Promega), pSNAPf (NEB), pEGFP-C1 (Clontech), pEF1a-mCherry (Clontech), and pCLIPf (NEB), respectively. These amplicons were then sub-cloned into the pcDH-DCP1A backbone to generate the appropriate plasmids.

Cell viability assays

100 μL of 10,000-20,000 cells were seeded per well of a 96 well white bottom plate or 96 well transparent plate in regular growth medium. 24 h after seeding, cells were treated with appropriate isotonic or hypertonic medium. Cell growth and viability were measured on the 96 well white bottom plate as an end point measurement for each time point and/or treatment using the Cell-titer GLO assay (Promega, # G7570) based on manufacturer's instructions. 96 well transparent plates were fixed with 100% methanol at RT for 10 min, stained with crystal violet (0.5% in 20% methanol) for 20 min at RT, washed with water and photographed.

Immunofluorescence

Cells were grown on 8 well chambered coverglasses (Thermo-Fisher, # 155383PK), washed with PBS, formaldehyde fixed and permeabilized using 0.5% Triton X-100 (Sigma, T8787-100ML) in 1x PBS at room temperature (RT) for 10 min. It is important that the tonicity of the wash buffer and fixative matched that of the cell medium. Cells were then treated with blocking buffer containing 5% normal goat serum (Jackson Immunoresearch, 005-000-121), 0.1% Tween-20 (Sigma, P9416-50ML) in 1x PBS at RT for 1 h. Primary antibodies were diluted in blocking buffer to appropriate concentrations. Cells were incubated with primary antibodies at RT for 1 h. Following three washes with the blocking buffer for 5 min each, cells were treated with secondary antibodies diluted in blocking buffer to appropriate concentrations. Then, following two washes with the blocking buffer and two washes with 1x PBS for 5 min each, cells were mounted in solution containing 10 mM Tris/HCl pH 7.5, 2 × SSC, 2 mM trolox, 50 μM protocatechuic acid, and 50 nM protocatechuate dehydrogenase. Mounts were overlaid with mineral oil and samples were imaged immediately.

Combined IF and RNA fluorescence *in situ* hybridization

Following the final 1x PBS washes in the abovementioned IF protocol, cells were formaldehyde fixed and permeablized overnight at 4°C using 70% ethanol. Cells were rehydrated in a solution containing 10% formamide and 2 × SSC for 5 min and then treated with 100 nM Oligo-dT30-Cy5 (IDT) for 16 h in 2 × SSC containing 10% dextran sulfate, 2 mM vanadyl-ribonucleoside complex, 0.02% RNase-free BSA, 1 μg/μl *E. coli* transfer RNA and 10% formamide at 37 °C. After hybridization, cells were washed twice for 30 min at 37 °C using a wash buffer (10% formamide in 2 × SSC). Cells were then mounted in solution containing 10 mM Tris/HCl pH 7.5, 2 × SSC, 2 mM trolox, 50 μM protocatechiuc acid, and 50 nM protocatechuate dehydrogenase. Mounts were overlaid with mineral oil and samples were imaged immediately.

Microscopy

Highly inclined laminated optical sheet (HILO) imaging was performed as described (Pitchiaya et al., 2012; Pitchiaya et al., 2017; Pitchiaya et al., 2013; Pitchiaya et al., 2019) using a cell-TIRF system based on an Olympus IX81 microscope equipped with a 60x 1.49 NA oil-immersion objective (Olympus), as well as 405 nm (Coherent, 100 mW at source, ~65 μW for imaging CB-Dex), 488 nm (Coherent ©, 100 mW at source, ~1.2 mW for imaging GFP), 561 nm (Coherent ©, 100 mW at source, ~50 μW for imaging mCh) and 640 nm (Coherent ©, 100 mW at source, 13.5 mW for imaging Cy5) solid-state lasers. Quad-band filter cubes consisting of z405/488/532/640rpc or z405/488/561/640rpc dichroic filters (Chroma) and z405/488/532/640 m or z405/488/561/640 m emission filters (Chroma) were used to filter fluorescence of the appropriate fluorophores from incident light. Emission from individual fluorophores was detected sequentially on an EMCCD camera (Andor IXon Ultra) for fixed cell imaging. For live cell imaging cells were seeded on Delta T dishes (Bioptechs, 04200417C) and imaged on a Bioptechs temperature control module (Bioptechs, 0420-4). High-throughput IF was performed on the same microscope using a 60x 0.9 NA air objective. The multi-well scanning mode in Metamorph®, the acquisition software, was used to control a motorized stage (MS-2000, Applied Scientific Instrumentation Inc.).

Image Analysis

For measuring the average GFP signal per cell, GFP intensity thresholds were set (Huang threshold in ImageJ) to automatically identify cell boundaries. Background intensity, outside of cell boundaries, was subtracted from GFP signal to extract the background corrected GFP intensity within cells. The corrected intensity was then divided by the total number of thresholded (Huang threshold in ImageJ) DAPI stained nuclei to extract the average GFP intensity per cell. For measuring the percentage of GFP signal within foci, images were first thresholded (percentage threshold in ImageJ) to create masks of foci and the GFP intensity within this mask was calculated. Background corrected foci intensity was then divided by the background corrected GFP intensity within cells. Average number of foci per cell in IF images were identified using the find maxima function in ImageJ. Briefly, a 5-pixel radius rolling ball was used to subtract the background from images, which were subsequently convolved with a 5x5 pixel kernel and a 2-pixel radius

Gaussian blur function. These image processing steps enhanced the definition of a spot that were easy to identify with the find maxima function. The noise tolerance (or threshold value) in the find maxima function was maintained across samples that were compared. The total number of spots was then divided by the number of nuclei to calculate the mean spots per cell. Imaris was used for single particle tracking. Custom MATLAB scripts were used to extract diffusion rates of the trajectories by fitting the mean squared displacement ($\langle r^2 \rangle$) over the first five observation time windows to a line and extracting the slope. Diffusion rates (D) were then calculated as per the 2-D diffusion equation from

$$\langle r^2 \rangle = 4 * D * t$$

The obtained logarithm of the obtained diffusion values was plotted as histograms in Origin which were then visualized as violin plots using custom scripts in MATLAB.

Intracellular GFP-DCP1A concentrations were determined using an eGFP calibration curve, obtained by capturing multi-frame movies of a range (1 nM – 30 μM) of EGFP dilutions in 1x PBS at the same camera acquisition settings used for imaging GFP-DCP1A. The average pixel intensity over 3 fields of view over 5 frames was fitted with a linear equation that was used to then assign mean intracellular GFP-DCP1A intensities to concentrations. In plots of foci number against concentration or intensity, the HOPS regime was drawn by defining the lowest concentration or intensity (x axis limit) that showed either > 100 foci or a threefold change in foci number under hypertonic treatment relative to isotonic, whichever was higher. The partition coefficient was calculated as:

$$PC = \frac{\sum I_{Foci}}{\sum I_{Cell}}$$

where I_{Foci} represent total intensity in foci in a cell, and I_{Cell} represents total intensity in the cell determined by semi-manual thresholding using custom scripts in MATLAB. The phase plot in Figure 2E was fit using a dose response equation in Origin:

$$y = A_1 - \frac{A_2 - A_1}{1 + 10^{(logx0 - x)p}}$$

The best fit to the binned data was used to determine the PC_{50}, given by log(x0). The hypertonic data were fit with p = 2 and isotonic data were fit with p = 1. All final figures were assembled in Adobe Illustrator.

Flow cytometry

Cell volume was evaluated using a Sony SH800 cell sorter on 100 μm sorting chips sheathed with 1x PBS (Life Technologies Applied Biosystems, Vic, Australia). Trypsinized U2-OS or UGD cell suspensions were treated with isotonic (150 mM Na^+) or hypertonic (300 mM Na^+) growth medium for 2 min, immediately fixed in pre-warmed (37°C) 4% paraformaldehyde solution with matched tonicity for 10 min at 25°C and washes 3 times with 1x PBS. Upon cell loading, GFP positive UGD cells were identified by fluorescence compensation from U2-OS cells via 488 nm illumination. GFP-gated cells were then analyzed for their forward scattering extent, since it is considered to related to the volume of the cell (Model, 2018).

RNA-seq and Bru-seq

For steady-state RNA-seq, UGD cells were grown in 10 cm dishes, treated with the appropriate medium (isotonic, 150 mM Na^+ or hypertonic, 300 mM Na^+) and cells were harvested by scraping in RIPA buffer (Thermo-Fisher, PI89900). Total RNA was then extracted with QIAGEN RNeasy midi kit (Cat. No. 75144). RNA integrity was assessed using an Agilent Bioanalyzer. Each sample was sequenced in duplicates using the Illumina HiSeq 2000 (with a 100-nt read length). Strand-specific paired-end reads were then inspected for sequencing and data quality (for example, insert size, sequencing adaptor contamination, rRNA content, sequencing error rate). Libraries passing quality control were trimmed of sequencing adaptors and aligned to the human reference genome, GRCh38. Sample were demultiplexed into paired-end reads using Illumina's bcl2fastq conversion software v2.20. Reads were mapped onto hg38 human reference genome using TopHat2. First the reference genome was indexed using bowtie2-build. Paired end reads were then aligned to the reference genome using TopHat2 with strand-specificity and allowing only for the best match for each read. Aligned file was used to calculate strand specific read count for each gene using bedtools multicov with -s option. A known genes gtf file downloaded from UCSC was used to calculate read count. Two additional bed files were created for each gene representing 10 kb upstream and 10 kb downstream of the TSS. For each gene, read count was calculated for its upstream and downstream region as well with strand-specificity. To estimate an RNA read-through event, we calculated the ratio of read count for 10 kb downstream of TSS to 10 kb upstream of TSS after normalizing it for gene expression and sequencing depth. A boxplot was plotted for this normalized ratio for the three samples using R software and ggplot2 package. Evaluation of significance was performed using the Student's t test. The aligned bam file of the sample was converted into bigwig format using deepTools bamcoverage. The resultant bigwig file was uploaded onto IGV for viewing of the RNA read-through event.

For Bru-seq, UGD cells were grown on T75 flasks to > 80% confluency. Flasks were washed once with fresh medium before bromouridine (BrU) treatment. BrU solution was diluted to a final concentration of 2 mM in McCoy's 5A medium containing 2% FBS containing 145 mM (isotonic) or 300 mM (hypertonic) monovalents. Cells were incubated in the appropriate bromouridine-containing medium for 30 min. Cells treated with hypertonic medium were allowed to recover in isotonic medium for 30 min or 6 h in

isotonic medium before they were harvested. Nascent transcript libraries for Bru-seq were prepared and sequenced as described (Paulsen et al., 2014).

Data from both RNA-seq and Bru-seq were analyzed as follows. We identified the transcription end sites (TES) of genes by GENCODE annotation and defined a 10 kb region upstream (US) and downstream (DS) of each TES, especially for genes that did not have any neighboring gene DS within the 10 kb distance. We then computed reads per kilobase million values for these US and DS bins and computed a DS/US ratio.

Chromatin Immunoprecipitation followed by sequencing (ChIP-seq) and analysis.

ChIP-seq experiments were carried out using the HighCell# ChIP-Protein G kit (Diagenode, Cat#: C01010063) following the manufacturer's protocol. Chromatin from five million cells was used per ChIP reaction with 6.5 μg of the target protein antibody. In brief, cells were exposed to isotonic (150 mM Na^+) or hypertonic (300 mM Na^+) conditions for 30 min, trypsinized in solutions that maintained tonicity and washed twice with 1x PBS (isotonic) or 2x PBS (hypertonic). This was followed by cross-linking for 12 min in 1% formaldehyde solution in iso- or hyperosmotic PBS (Sigma-Aldrich, Cat#: F8775-25ML). Crosslinking was terminated by the addition of 1/10 volume 1.25 M glycine for 5 min at room temperature. This was followed by cell lysis and sonication (Bioruptor, Diagenode) resulting in an average chromatin fragment size of 200 bp. Fragmented chromatin was used for immunoprecipitation using various antibodies with an overnight incubation at 4°C. Immunoprecipitated DNA was de-crosslinked and purified using the iPure Kit V2 (Diagenode, Cat#: C03010015) using the manufacturer's protocol. Purified DNA was quantified using Qubit-3 (Invitrogen) and 10-100 ng of total DNA was used for library preparation using the KAPA Hyper Prep kit (KAPABiosystems, Cat#: KK8500) as per the manufacturer's protocol. Briefly, DNA was first converted to blunt-ended fragments via end-repair and a single 'A' nucleotide was added to fragment ends. This was immediately followed by ligation of Illumina adaptors and PCR amplification (for 9-12 cycles) using Illumina barcoding primers and Phusion DNA polymerase (NEB, Cat# M0530S). PCR products were double size-selected using the KAPA Pure beads (Roche, Cat#: 07983280001) to remove fragments larger than 500 bp (0.65X beads:sample ratio) and primer dimers (0.9X beads:sample ratio). In the end, all libraries were quantified and quality checked using the Bioanalyzer 2100 (Agilent) and sequenced on the Illumina HiSeq 2500 Sequencer (paired-end, 50-nucleotide read length) to yield roughly 30-40 million total reads.

ChIP-Seq reads were aligned to the human reference genome (GRC h38/hg38) with the Burrows-Wheeler Aligner (BWA 0.7.17-r1198) (Li and Durbin, 2009). The SAM file obtained after alignment was converted into BAM format using SAMTools (Version: 1.9) (Li et al., 2009). Using deepTools bamCoverage (Ramírez et al., 2016), a coverage file (bigWig format) for each sample was created. The coverage is calculated as the number of reads per bin, where bins are short consecutive counting windows. While creating the coverage file, the data was normalized with respect to each library size. DeepTools computeMatrix was used to calculate scores per genome regions. We used PolyASite 2.0 (Herrmann et al., 2020) to determine the locations of polyA sites on terminal exons across the human genome. These locations were used as the genome regions while running computeMatrix and calculating scores for each sample across these sites and a 1-kb window up- and downstream of these regions. To create a profile plot for scores over these polyA sites, we used deepTools plotProfile. The score matrix generated using computeMatrix was the input for plotting the score profile.

QUANTIFICATION AND STATISTICAL ANALYSIS

Graphpad-Prizm and Origin were used for statistical analysis and plotting. For pairwise comparisons, p values were calculated based on non-parametric unpaired t tests with a Kolmogorov-Smirnov test. For comparisons involving more than 2 samples, one-way-ANOVA tests were used with a Geisser-Greenhouse correction. In general p values < 0.05 were considered significant. Specific p values for pairwise comparisons are reported in figures and their respective figure legends.

Molecular Cell, Volume *79*

Supplemental Information

Multivalent Proteins Rapidly and Reversibly Phase-Separate upon Osmotic Cell Volume Change

Ameya P. Jalihal, Sethuramasundaram Pitchiaya, Lanbo Xiao, Pushpinder Bawa, Xia Jiang, Karan Bedi, Abhijit Parolia, Marcin Cieslik, Mats Ljungman, Arul M. Chinnaiyan, and Nils G. Walter

SUPPLEMENTARY FIGURES AND LEGENDS

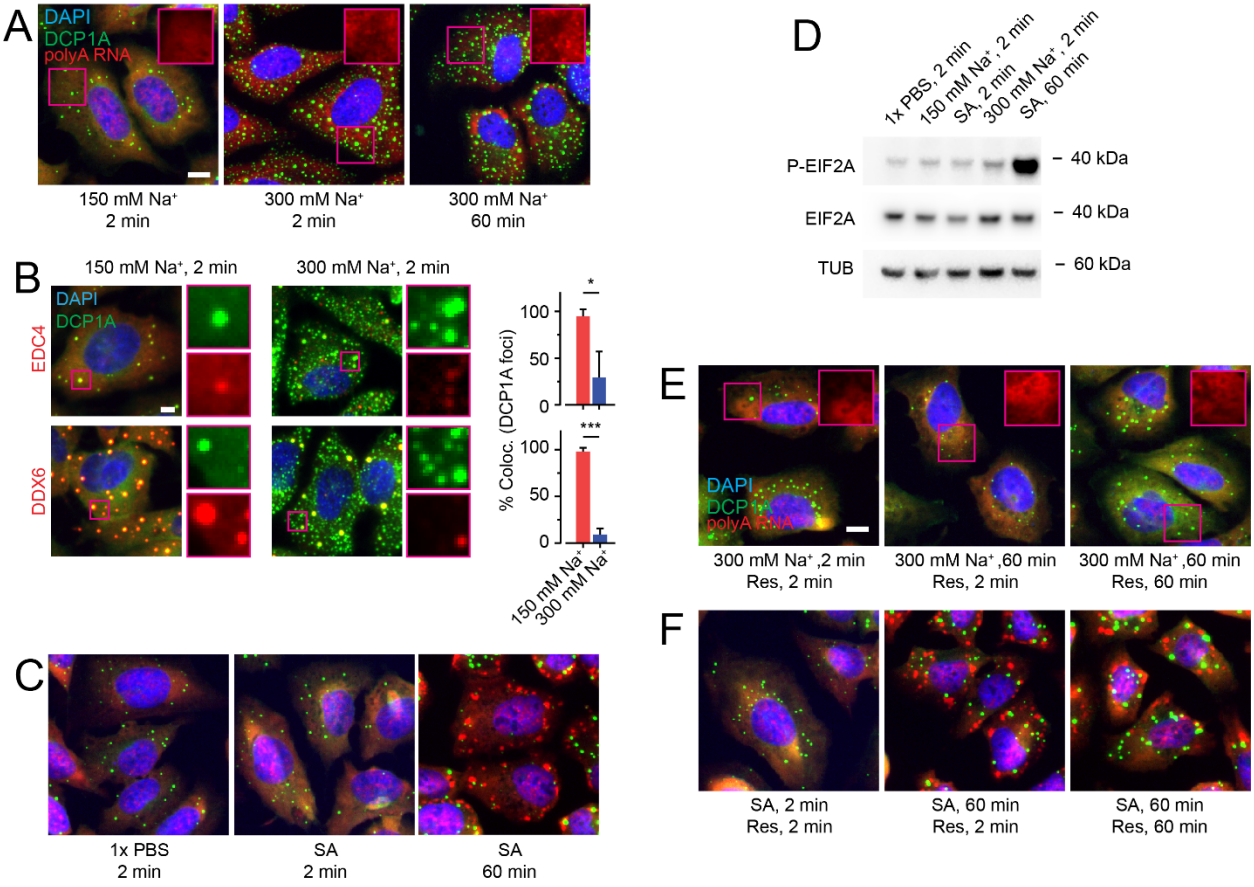

Figure S1. Hypertonicity-induced DCP1A foci are not canonical PBs or SGs. Related to Figure 1. (A) Representative pseudocolored, combined IF – RNA-FISH images of U2-OS cells stained for DAPI (blue), DCP1A (green) and polyA RNA (red) at various time points after isotonic (150 mM Na^+) or hypertonic (300 mM Na^+) medium addition. Scale bar, 10 μm. (B) Representative pseudocolored IF images of U2-OS cells stained for DAPI (blue), DCP1A (green), and EDC4 (top panels, red) or DDX6 (bottom panels, red) as indicated, treated with isotonic (150 mM Na^+) or hypertonic (300 mM Na^+) medium for 2 min. Scale bar, 10 μm. The plots represent the fraction of DCP1A foci colocalizing with EDC4 or DDX6 foci under each condition. n = 3, 50 cells, *$p < 0.01$, ***$p < 0.0001$, significance by two-tailed, unpaired Student's t-test. (C) Representative

pseudocolored, combined IF – RNA-FISH images of U2-OS cells stained for DAPI (blue), DCP1A (green) and polyA RNA (red), and either mock treated with 1x PBS or treated with 0.5 mM SA for the appropriate time points. (D) Western blot of phosphorylated EIF4E (P-EIF4E), EIF4E and tubulin upon various osmotic and SA perturbations. (E-F) Representative pseudocolored, combined IF – RNA-FISH images of U2-OS cells stained for DAPI (blue), DCP1A (green) and polyA RNA (red). Scale bar, 10 μm. (E) Cells were first treated with hypertonic (300 mM Na+) medium for the appropriate time points and then rescued with isotonic (150 mM Na+) medium for various durations. (F) Cells were first treated with 0.5 mM SA for the appropriate time points and then rescued with medium containing 1x PBS for various durations.

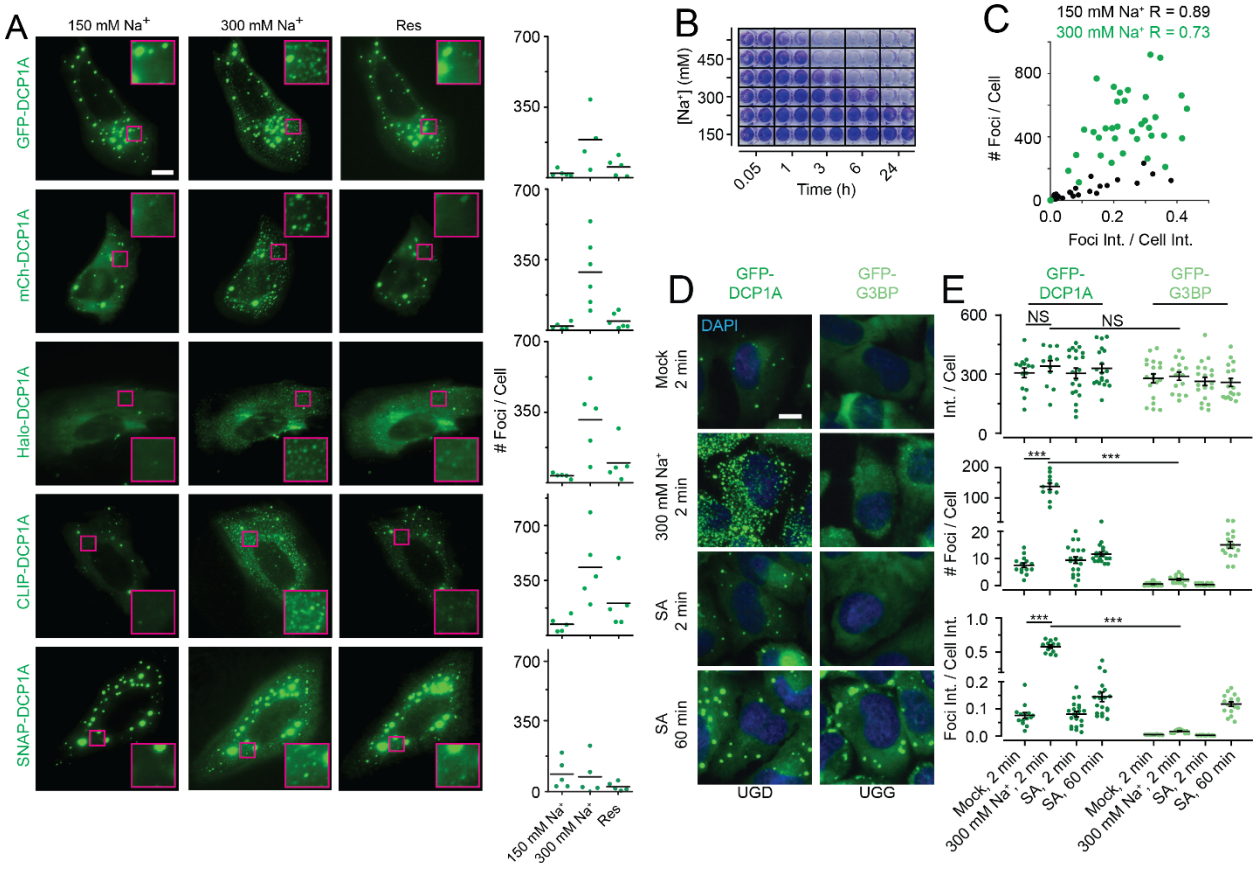

Figure S2. Rapid and reversible condensation of DCP1A does not depend on the fusion tag, does not affect cell viability and is distinct from G3BP condensation. Related to Figure 2. (A) Representative pseudocolored images of U2-OS cells expressing DCP1A fused to different types of fluorescent or fluorogenic tags (green). Cells were treated with isotonic (150 mM Na^+, 2 min) medium, hypertonic (300 mM Na^+, 2 min) medium, or rescued with isotonic medium (2 min) after hypertonic treatment (2 min). Scale bar, 10 μm. Scatter plot of the number of foci per cell for each treatment condition is also shown. n = 2, > 5 cells per sample. (B) Representative image of a 96-well plate probed for cell viability by crystal violet staining across various Na^+ concentrations and multiple time points. n = 3, with technical replicates for each n. (C) Correlation plot of the number of foci per cell against the partition coefficient in the same

cell. R = correlation coefficient. Black data points = 150 mM Na^+ treatment, green data points = 300 mM Na^+ treatment. (D) Representative pseudocolored images of cells stably expressing GFP-DCP1A (UGD, green) or GFP-G3BP (UGG, green) and subjected to osmotic or SA stress for various amounts of time. After fixation, cells were stained with DAPI (blue). Scale bar, 10 μm. (E) Scatter plots of area normalized cell intensity (top), number of foci per cell (middle) and partition coefficient (bottom). Each dot represents a cell. Line, mean, error bars, standard error. n = 3, > 15 cells per condition, NS = not significant, ***$p < 0.0001$, significance by two-tailed, unpaired Student's t-test.

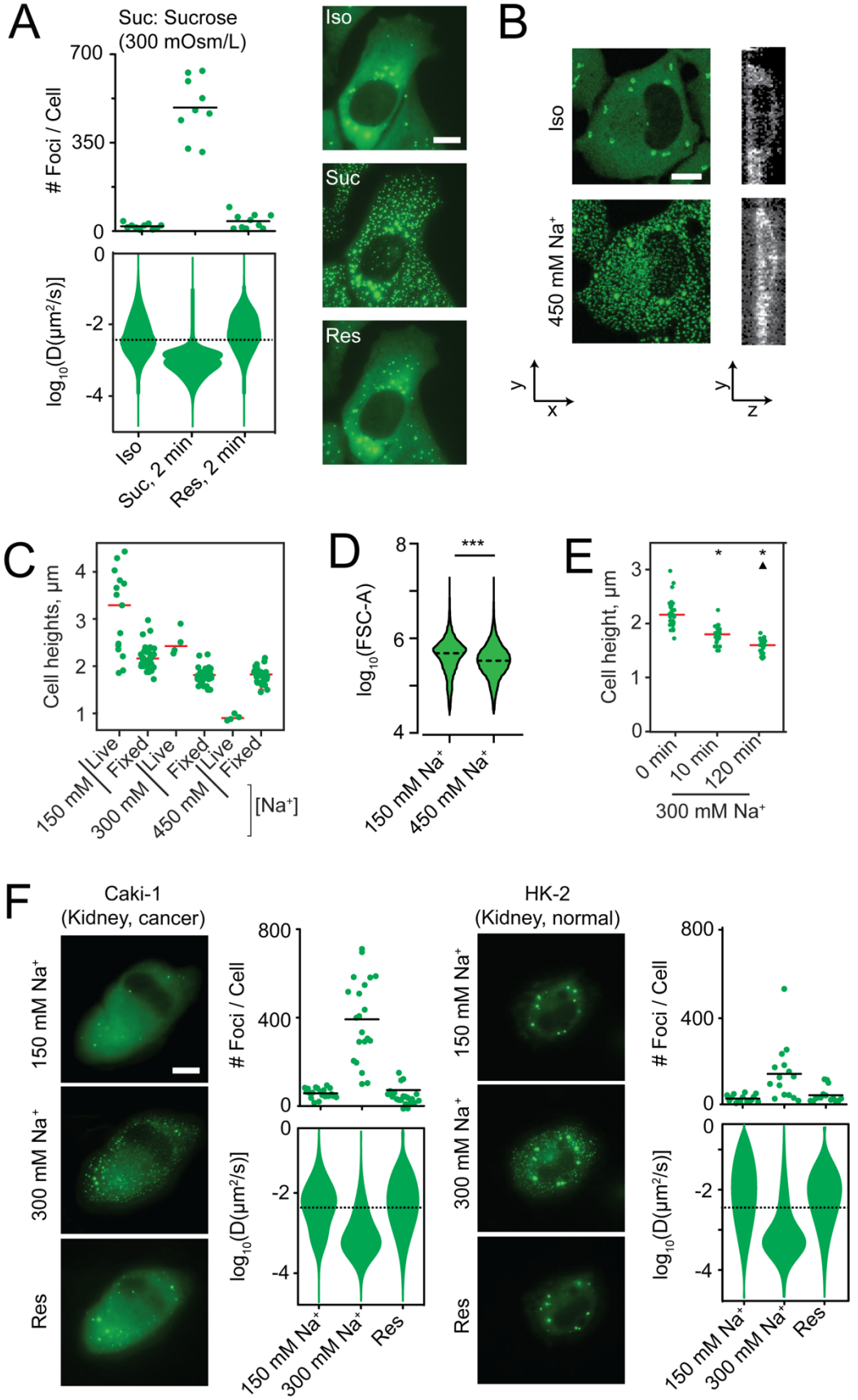
A
Suc: Sucrose
(300 mOsm/L)
Foci / Cell
700
350
0
log10(D(μm²/s))
0
-2
-4
Iso
Suc, 2 min
Res, 2 min
Iso
Suc
Res
B
Iso
450 mM Na+
y
x
y
z
C
Cell heights, μm
4
3
2
1
Live
Fixed
150 mM
300 mM
450 mM
[Na+]
D
log10(FSC-A)
8
6
4
***
150 mM Na+
450 mM Na+
E
Cell height, μm
3
2
1
0
*
*
0 min
10 min
120 min
300 mM Na+
F
Caki-1
(Kidney, cancer)
HK-2
(Kidney, normal)
150 mM Na+
300 mM Na+
Res
Foci / Cell
800
400
0
log10(D(μm²/s))
0
-2
-4
150 mM Na+
300 mM Na+
Res

Figure S3. Hyperosmotic phase separation of DCP1A is correlated with cellular compression and is independent of cell type. Related to Figure 3. (A) Scatter plot of the number of foci per cell (top), violin plots of diffusion constants associated with DCP1A foci (bottom). Representative pseudocolored images of UGD cells (GFP, green) were treated with isosmotic (Iso) growth medium, hyperosmotic growth medium containing the non-ionic osmolyte Sucrose (Suc, 2min) or rescued (Res) with isosmotic medium (2 min) after sucrose treatment (2 min). n = 2, > 5 cells per sample. Scale bar, 10 μm. (B) Representative x-y (green) and y-z (gray) projection of a UGD cell from 3-D imaging assay wherein the cell was treated with isotonic (150 mM Na^+) medium or hypertonic (300 mM Na^+) medium. n = 1, 4 cells per sample. Scale bars, 10 μm (x and y) and 5 μm (z). (C) Scatter plots representing cell heights measured by DiI staining and 3-D imaging in live- and fixed-cells. Cell heights were measured from YZ sections of Z-stack images of UGD. n=2, >8 cells per replicate. (D) Violin plots of forward scatter from fixed UGD cells as measured by flow-cytometry. Cells were treated with isotonic (150 mM Na^+) or hypertonic (300 mM Na^+) medium for 2 min. n = 3, > 50,000 events per condition, ***$p < 0.0001$, significance by two-tailed, unpaired Student's t-test. Dotted line, median. (E) Scatter plots representing cell heights measured by DiI staining and 3-D imaging in fixed-cells. Cells were treated with hypertonic (300 mM Na^+) medium prior to fixation. Cell heights were measured from YZ sections of Z-stack images of UGD, n=2, >8 cells per trial. (F) Representative pseudocolored images of Caki-1 or HK-2 cells expressing GFP-DCP1A (green). Cells were treated with isotonic (150 mM Na^+, 2 min) medium, hypertonic (300 mM Na^+, 2 min) medium or rescued with isotonic medium (2 min) after hypertonic treatment (2 min). Scale bar, 10 μm. Scatter plot of the number of foci per cell (top) and

violin plots of diffusion constants associated with DCP1A foci (bottom) for each treatment condition for Caki-1 or HK-2 cells are also shown. n = 2, > 5 cells per sample.

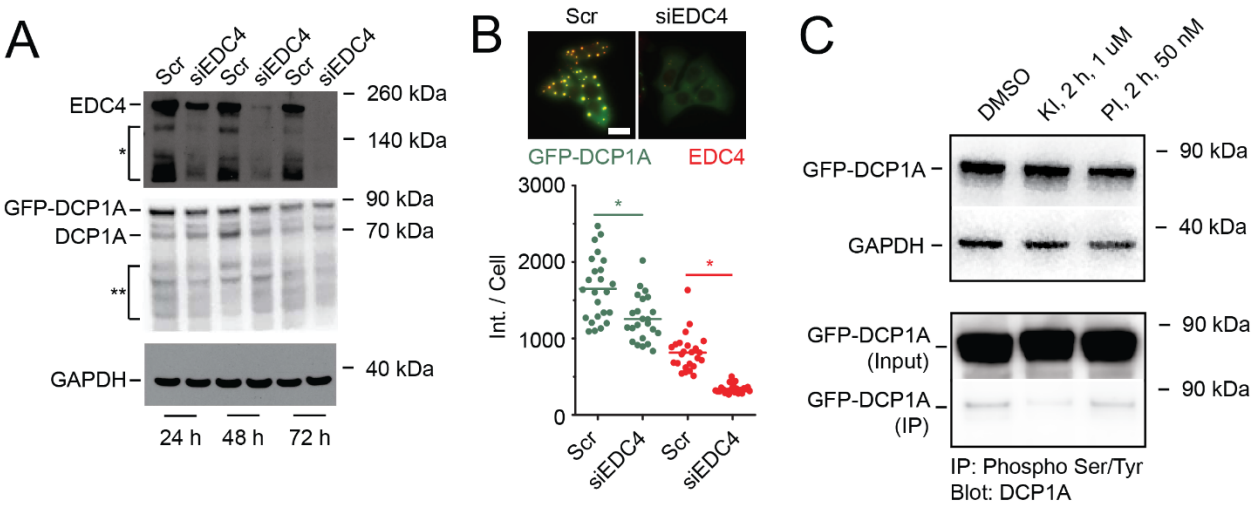

Figure S4. Knockdown of EDC4 results in reduced expression of DCP1A, but kinase inhibitor treatment only reduced DCP1A phosphorylation. Related to Figure 4. (A) Western Blot of EDC4, DCP1A, and GAPDH after various siRNA treatment times (24, 48 and 72 hr post siRNA transfection). Bands labeled with "*" and "**" were detected by EDC4 and DCP1A antibodies respectively and either denote non-specific bands or shorter protein fragments. (B) Representative pseudocolored IF images of UGD cells (top) expressing GFP-DCP1A (green), stained for EDC4 (red). Scale bar, 20 μm. Cells were either transfected with a scrambled siRNA (Scr) or siEDC4 for 48 h. Scatter plot (bottom) of the average intensity of GFP (green) or EDC4 (Cy5, red) per UGD cell transfected with a scrambled siRNA (Scr) or siEDC4 in isotonic conditions. n = 2, > 20 cells per sample, *p ≤ 0.01, by two-tailed, unpaired Student's t-test. (C) Western blot of DCP1A, and GAPDH after various drug perturbations (top). Western blot of DCP1A after immunoprecipitation with phospho-specific antibody, upon various drug perturbations (bottom).

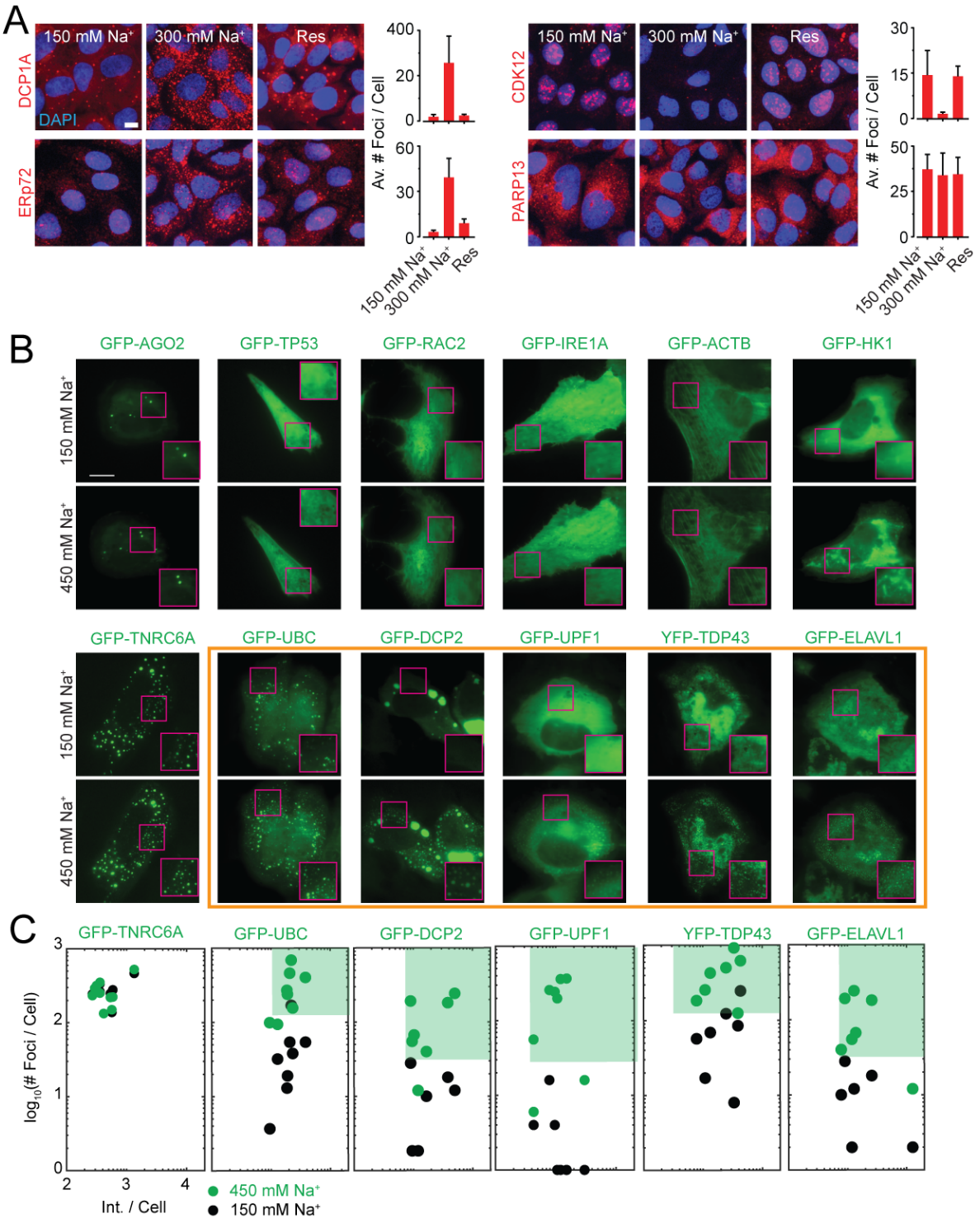

Figure S5. High-thoughput IF and GFP imaging of proteins in U2OS cells. Related to Figure 5. (A) Representative pseudocolored images of U2OS cells stained with the appropriate antibody (red, DCP1A, ERp72, CDK12, PARP13). Cells were treated with isotonic (150 mM Na^+) medium

(2 min), hypertonic (300 mM Na^+) medium (2 min) or rescued (res) with isotonic medium (2 min) after hypertonic treatment (2 min). Scale bar, 10 μm. Quantification of the average number of foci per cell is also depicted. Error bar, standard deviation. n = 3, > 50 cells. (B) Representative pseudocolored images of U2OS cells (GFP, green) transfected with the appropriate GFP-tagged construct and treated with isotonic (150 mM Na^+) medium or hypertonic (300 mM Na^+) medium for 2 min. Scale bar, 10 μm. Inset depicts a zoomed-in area corresponding to a 15 x 15 μm^2 magenta box. Constructs that exhibit HOPS are highlighted in orange. (C) Scatter plot of the number of foci per cell against the area-normalized total cell fluorescence intensity for each GFP-labeled protein. n = 2, > 5 cells per sample. The green contour depicts HOPS.

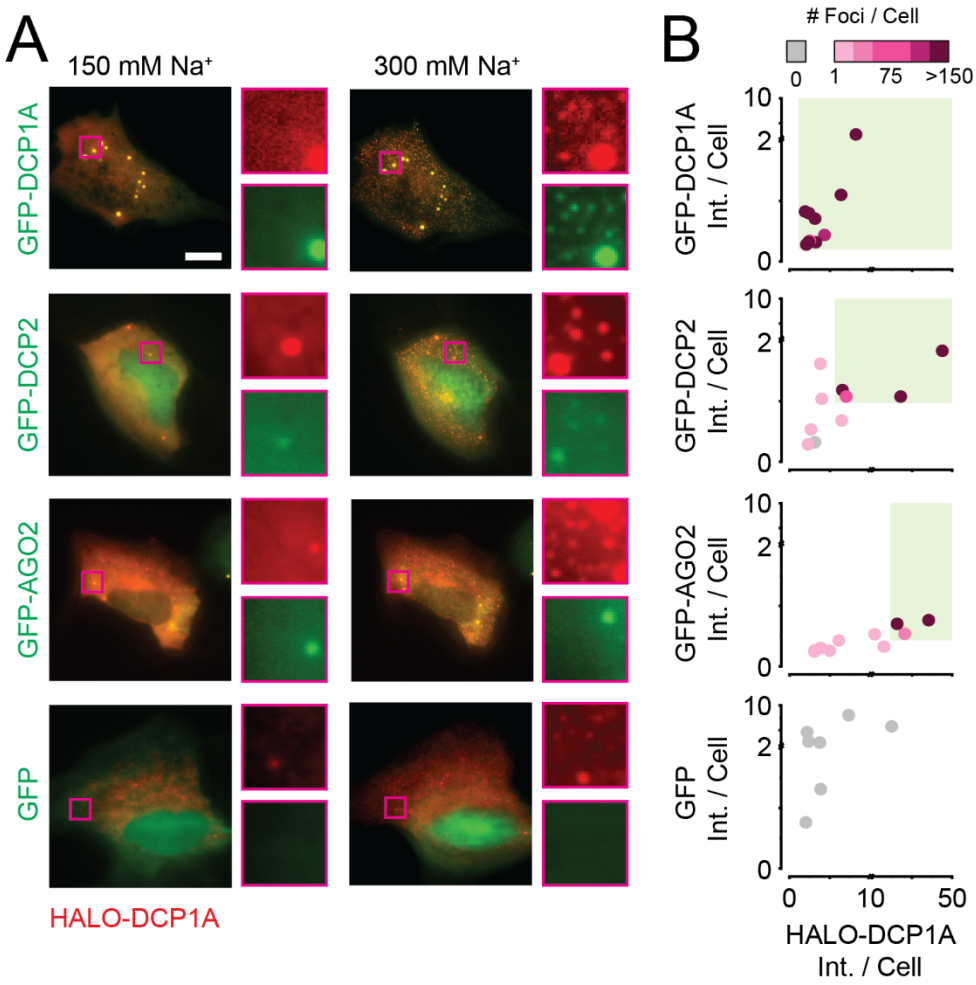

Figure S6. Interactors of DCP1A can exhibit HOPS at high DCP1A concentration. Related to Figure 5. (A) Representative pseudocolored images of U2OS cells (GFP, green, JF646, red) transfected with GFP-tagged DCP1A (positive control), DCP2, AGO2, or GFP (negative control) and treated with isotonic (150 mM Na^+) or hypertonic (300 mM Na^+) medium for 2 min. Scale bar, 10 μm. Insets depict magnified areas corresponding to a 2 x 2 μm^2 box as indicated; n = 2, 5 cells per replicate. (B) Color mapped scatter plots of area normalized Halo-DCP1A fluorescence intensity against area normalized GFP-tagged protein intensity. Each dot represents a cell and its color represents the number of foci within the cell upon hypertonic (300 mM Na^+) treatment. The color scheme is provided on the top of the plot. Green contours depict HOPS conditions, which is defined

by an at least 3-fold increase in the number of foci under hypertonic conditions compared to isotonic controls.

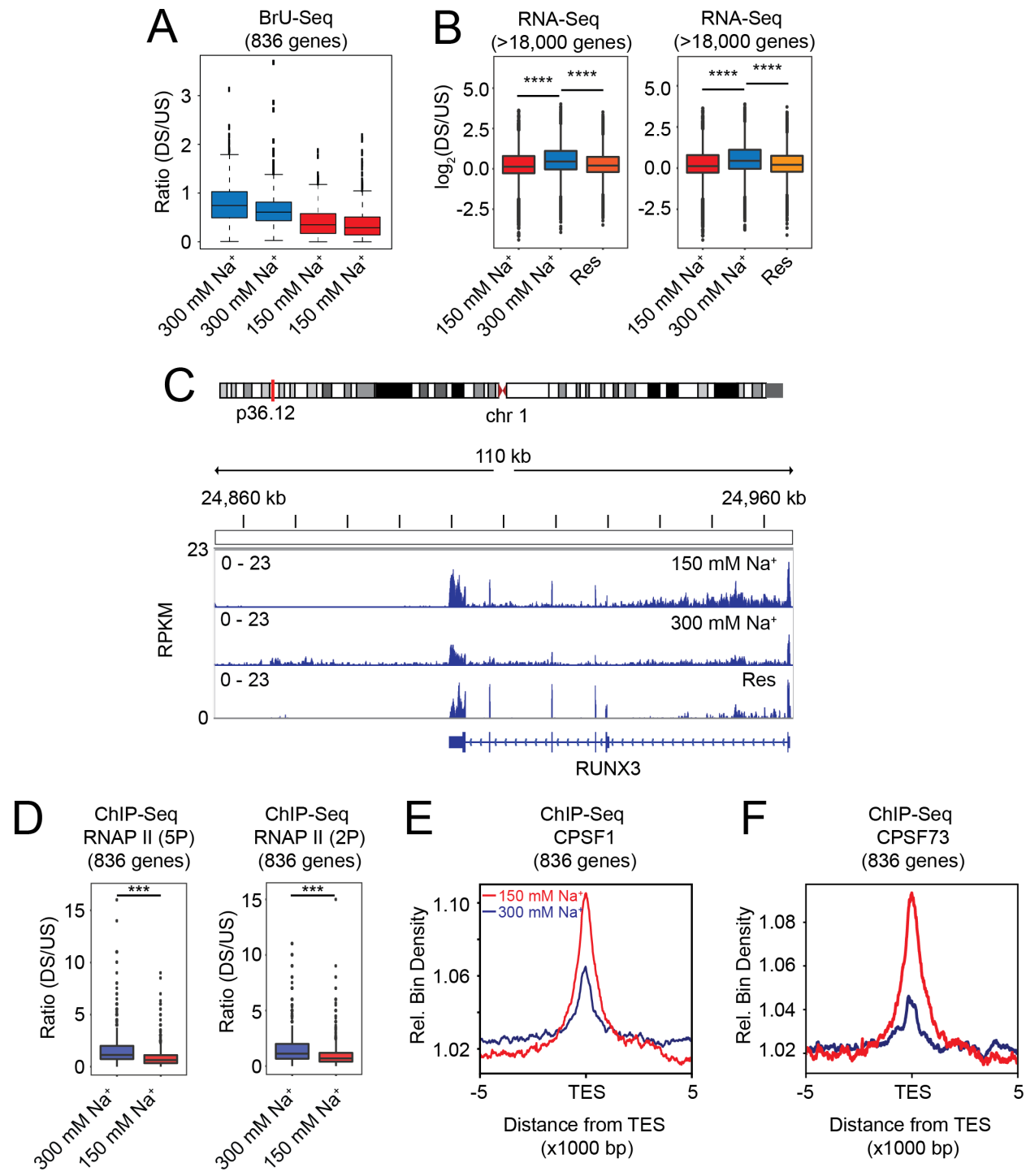

Figure S7. Hyperosmolarity-induced transcript read-through correlates with loss of TES occupancy by CPSFs. Related to Figure 6. (A) Ratio between read counts

downstream (DS) and read-counts upstream (US) of TES for 836 genes assayed by BrU-Seq for each replicate. Cells were treated with isotonic (150 mM Na^+, 30 min) or hypertonic (300 mM Na^+, 30 min) mediums prior to sequencing. (B) DS:US ratio of > 18,000 genes that show transcript read-through in RNA-Seq assays. Cells were treated with isotonic (150 mM Na^+, 4 h) medium, or hypertonic (300 mM Na^+, 4 h) medium, or rescued (Res) with isotonic medium (4 h) after hypertonic treatment (4 h) prior to sequencing. (C) RNA-seq tracks of the RUNX3 locus under isotonic (150 mM Na^+, 4 h) medium, hypertonic (300 mM Na^+, 4 h) medium, or rescued (Res) with isotonic medium (4 h) after hypertonic treatment (4 h) prior to sequencing. (D) Ratio between ChIP-seq read counts downstream (DS) and upstream (US) of TES for 836 genes. Left panel, ChIP-seq with antibody against Serine 5P in C-terminal domain (CTD) of RNA Pol II; right panel, ChIP-seq with antibody against Serine 2P in CTD of RNA Pol II. Cells were treated with isotonic (150 mM Na^+, 30 min) or hypertonic (300 mM Na^+, 30 min) medium prior to ChIP-seq. (E and F) Aggregated ChIP-seq reads of CPSF1 (E) and CPSF73 (F) for 836 genes mapped around the TES. Cells were treated with isotonic (150 mM Na^+, 30 min, red) or hypertonic (300 mM Na^+, 30 min, blue) medium prior to ChIP-seq.